SUPPLEMENTARY ONLINE MATERIAL

Aluminum Textile-Based Binder-Free Nanostructured Battery Cathodes Using a Layer-by-Layer Assembly of Metal/Metal Oxide Nanoparticles

Donghyeon Nam[1], Minseong Kwon[1], Yongmin Ko[2], June Huh[1], Seung Woo Lee[3,a)], and Jinhan Cho[1,b)]

AFFILIATIONS

[1]Department of Chemical and Biological Engineering, Korea University, 145 Anam-ro, Seongbuk-gu, Seoul 02841, Republic of Korea

[2]Division of Energy Technology, Materials Research Institute, Daegu Gyeongbuk Institute of Science and Technology (DGIST), 333 Techno Jungang-daero, Hyeonpung-eup, Dalseong-gun, Daegu, 42988, Republic of Korea

[3]The George W. Woodruff School of Mechanical Engineering, Georgia Institute of Technology, Atlanta, Georgia 30332, USA

Author to whom correspondence should be addressed: [a)]seung.lee@me.gatech.edu, [b)]jinhan71@korea.ac.kr

Necessity of the Ni sublayer for Al electroplating

Al electroplating of (Au NP/DETA)$_4$-coated polyester textiles was conducted after preplating of a small thickness Ni sublayer. First, Al electroplating without a Ni sublayer was investigated to confirm the necessity of the Ni sublayer. Direct Al electroplating on the (Au NP/DETA)$_{10}$-coated polyester textiles was conducted at a current density of 250 mA cm^{-2}. In the case of the (Au NP/DETA)$_{10}$-coated polyester textiles, decomposition of the ionic liquid occurred at a current density above 30 mA cm^{-2} due to the high voltage induced by the relatively high electrical resistivity of the (Au NP/DETA)$_{10}$-coated polyester textiles despite the high bilayer number. Unfortunately, electroplating at low current density has been reported to tend to produce coarse-grained surfaces through dendritic growth.[S1] As shown in **Fig. S5(a)**, the microsized pores of (Au NP/DETA)$_{10}$-coated polyester textiles were covered by clustered Al dendrites. Moreover, the irregular dendritic growth initially blocked the outer pores, causing a vertical gradient of Al distribution from the exterior to interior of the polyester textile substrate (**Fig. S5(b)**,). Therefore, Ni electroplating was conducted on (Au NP/DETA)$_4$-coated polyester textiles to readily reduce the sheet resistance to below 1 Ω sq^{-1} (~0.5 Ω sq^{-1}), even lower than that of (Au NP/DETA)$_{10}$-coated polyester. We were able to conduct Al electroplating with a current density up to 180 mA cm^{-2} on Ni-electroplated (Au NP/DETA)$_4$-coated polyester textiles (i.e., Ni-ETs) without any decomposition of the ionic liquid. As shown in **Fig. S7**,, the Al electroplating conditions were optimized to a current density of 120 mA cm^{-2} and an electroplating time of 10 min, exhibiting a remarkably high conductivity of 2310 S cm^{-1} (sheet resistance ~ 0.025 Ω sq^{-1}).

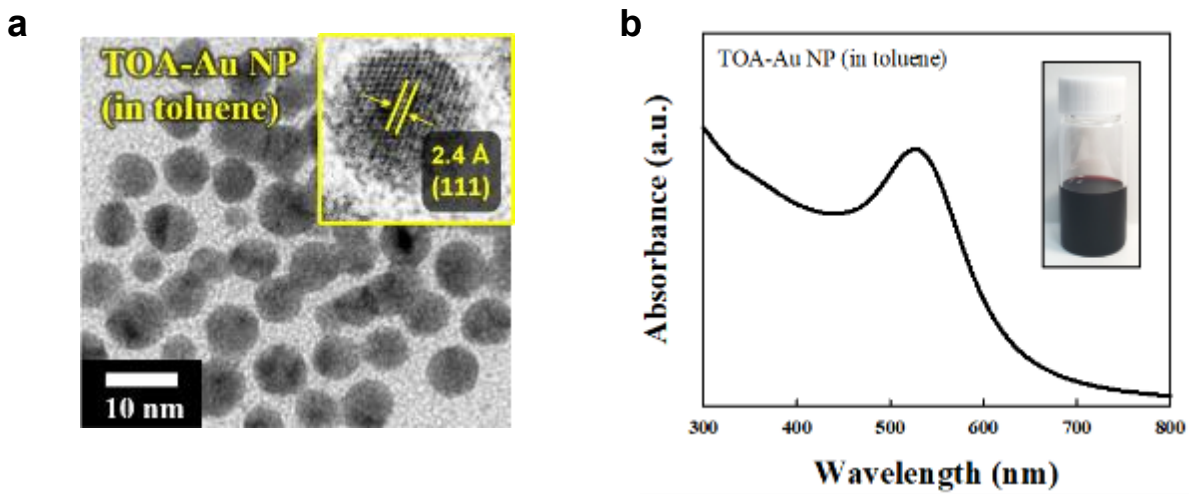

FIG. S1. (a) High-resolution transmission electron microscopy (HR-TEM) image and (b) UV-vis spectrum of TOA- Au NPs with a diameter of approximately 7 nm and photographic image of TOA-Au NP solution (in toluene) (inset).

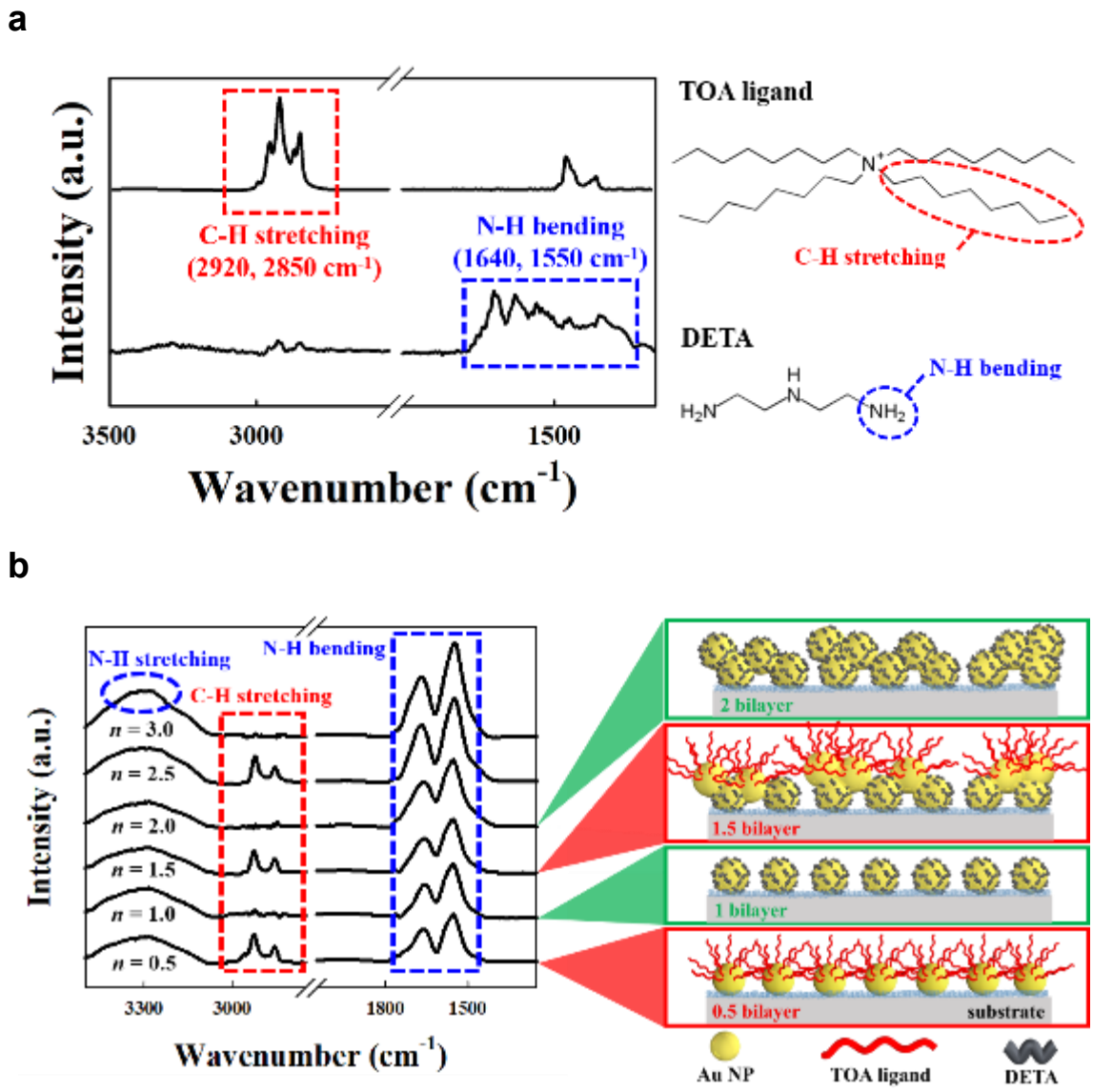

FIG. S2. (a) FT-IR spectra of TOA-Au NP and DETA. The C—H stretching peaks at 2928 and 2856 cm^{-1} originate from long alkyl chains of bulky TOA ligands. On the other hand, the absorption peaks at 3300, 1654, and 1554 cm^{-1} are designated as N—H stretching and bending peaks of DETA. (b) FTIR spectra and scheme of ligand-exchange LbL-assembled (Au NP/DETA)$_n$ multilayers as a function of the bilayer number (n). As shown in the FTIR spectra of Figure S2b, the deposition of DETA onto the TOA-Au NP-coated-substrates gradually eliminated the bulky TOA ligands (see the C-H stretching peaks at 2,850 − 2,950 cm^{-1}) loosely bound to the surface of the Au NPs because the amine moieties of DETA (see the -N-H stretching peaks at 3,300 − 3,400 cm^{-1} and N-H bending peaks at 1,540 − 1,650 cm^{-1}) as an electron donor had a higher affinity (by covalent bonding) for the surface of the various metal

or metal oxide NPs and Au NPs, than for functional groups such as the ammonium groups of the TOA ligands. Therefore, the alternating deposition of DETA and TOA-Au NPs repeated the generation and disappearance of the C-H stretching peaks (at 2,850 − 2,950 cm^{-1}) originating from the TOA ligands when the outermost layer was changed from DETA to TOA-Au NPs and vice versa.

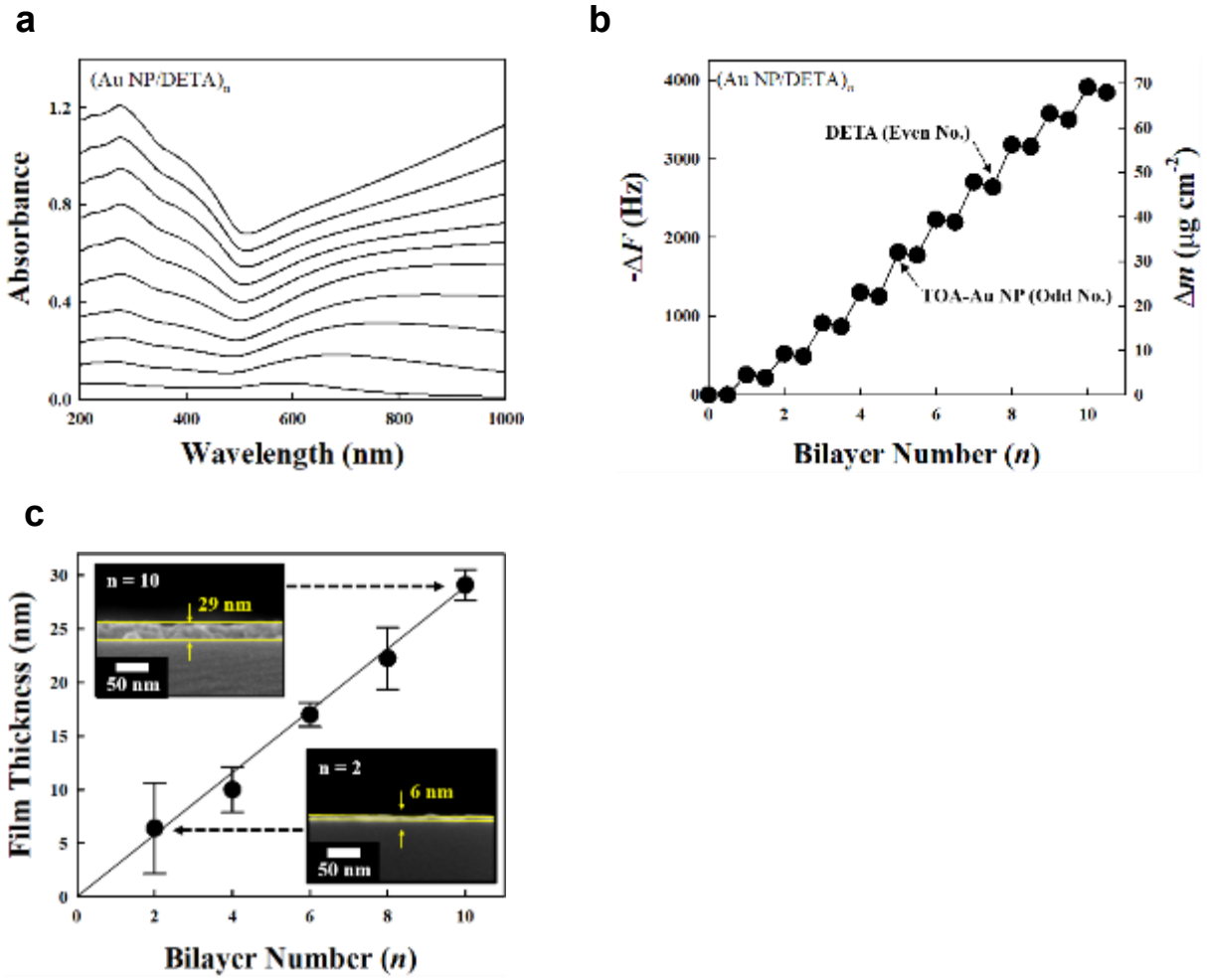

FIG. S3. LbL growth of (Au NP/DETA)$_n$ multilayers. (a) UV-vis spectroscopy of (Au NP/DETA)$_n$ multilayers onto quartz substrate. With increasing bilayer number (n), the surface plasmon absorption peak of LbL-assembled TOA-Au NPs was strongly red-shifted, and then completely disappeared with increasing bilayer number. These phenomena originate from the formation of closely packed Au NP arrays in lateral and vertical dimension. (b) QCM data of (Au NP/DETA)$_n$ multilayers as a function of layer number. Alternating the deposition of TOA-Au NPs and DETA resulted in $-\Delta F$ of 415.9 ± 70 (mass change (Δm) of ~ 7.34 μg·cm^{-2}) and –33.3 ± 16 Hz (Δm of ~ 0.588 μg·cm^{-2}) per layer, respectively. Particularly, a decrease of $-\Delta F$ (or Δm) during the deposition of DETA imply the ligand exchange between bulky TOA ligands (M_w ~ 322 g mol^{-1}) and small DETA linkers (M_w ~ 103 g mol^{-1}). (c) Film thickness of (Au NP/DETA)$_n$ multilayers adsorbed onto silicon wafer. With increasing the bilayer number (n) from 2 to 10, the total film thicknesses of (Au NP/DETA)$_n$ multilayers increased from 6 to 29 nm. Although the average thickness per bilayer (approximately 2.9 nm) was thinner than the

diameter (~ 7 nm) of Au NP, the sufficient surface coverage of Au NPs could be improved with increasing the number of LbL deposition.

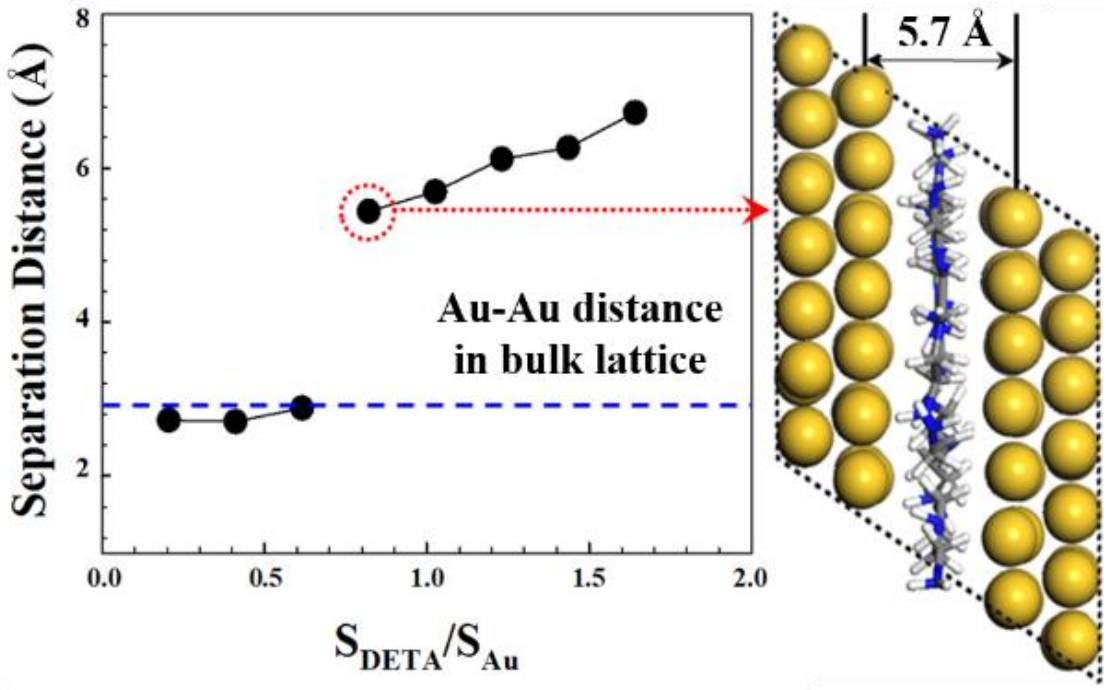

FIG. S4. DFT-computed adsorption energy (E_{abs}) of DETA linker between Au surfaces as a function of separation distance (h). The blue dashed line represents the adsorption energy of DETA on the single Au surface. Inset: Geometry-optimized molecular structure of DETA at the separation distance h = 5.7 Å.

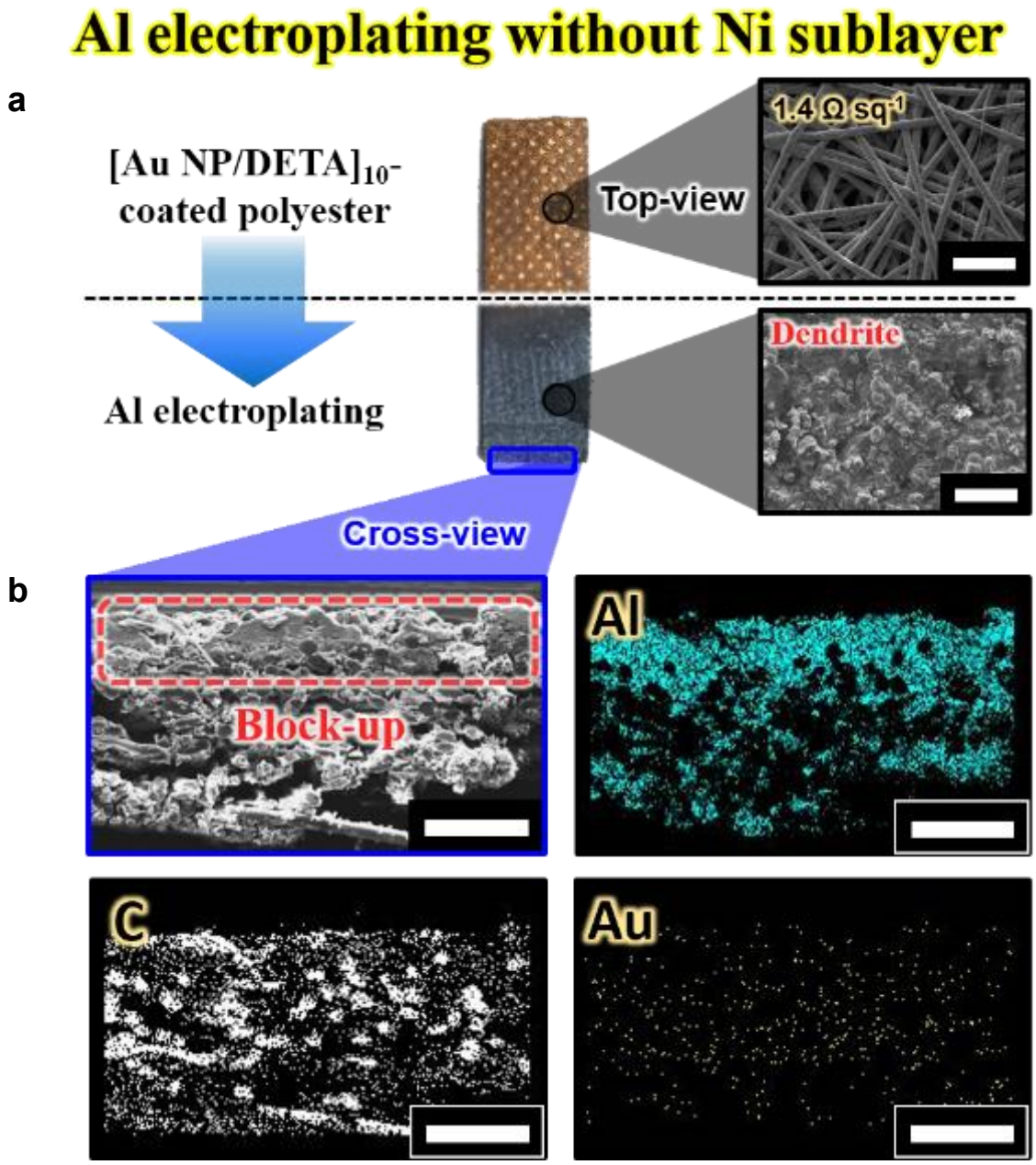

FIG. S5. (a) The photographic and top-view FE-SEM images (scale bar, 150 μm) of the (Au NP/DETA)$_{10}$ multilayer-coated polyester (i.e, (Au NP/DETA)$_{10}$/polyester) and Al electroplated (Au NP/DETA)$_{10}$/polyester (i.e, Al/(Au NP/DETA)$_{10}$/polyester). In this case, dendrites from Al electroplating were grown to become clusters blocking the porous structure of the polyester substrates. (b) The cross-view FE-SEM and corresponding EDS mapping images of Al/(Au NP/DETA)$_{10}$/polyester (scale bar, 100 μm). In this case, the exterior parts of the Al/(Au NP/DETA)$_{10}$/polyester were blocked by Al clusters inducing gradients of Al electroplating from exterior to interior part of the polyester substrates.

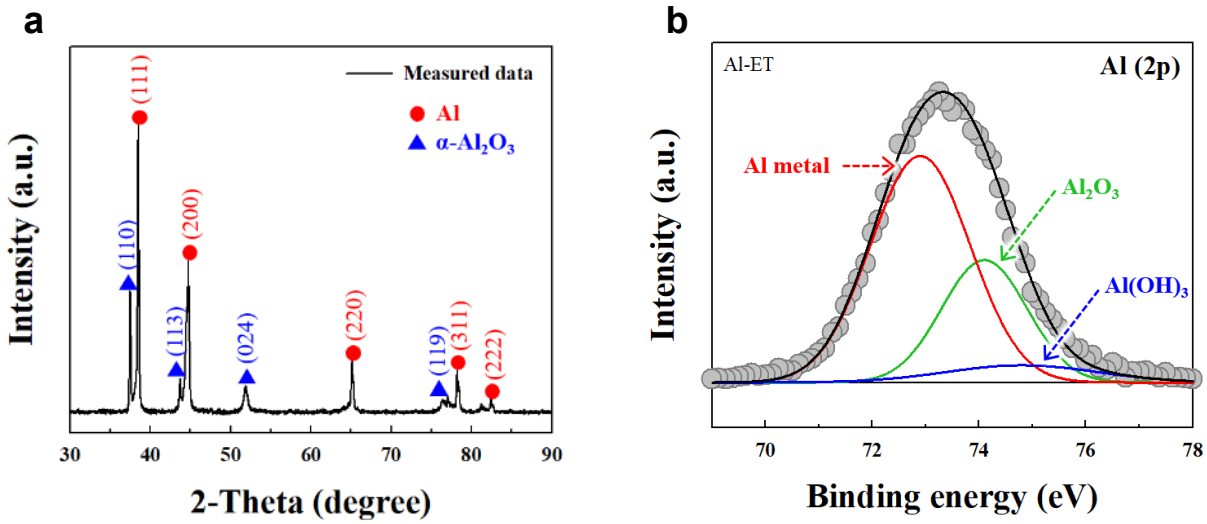

FIG. S6. (a) XRD data of the Al-electroplated polyester textile. Red circles and blue triangles indicated the diffraction peaks originating from Al and α-Al_2O_3, respectively. The XRD pattern of the Al-electroplated polyester textile exhibited the characteristic (111), (200), (220), (311), and (222) peaks of Al and (110), (113), (024), and (119) peaks of α-Al_2O_3. (b) Deconvoluted XPS spectra of Al 2p collected from Al-ET.

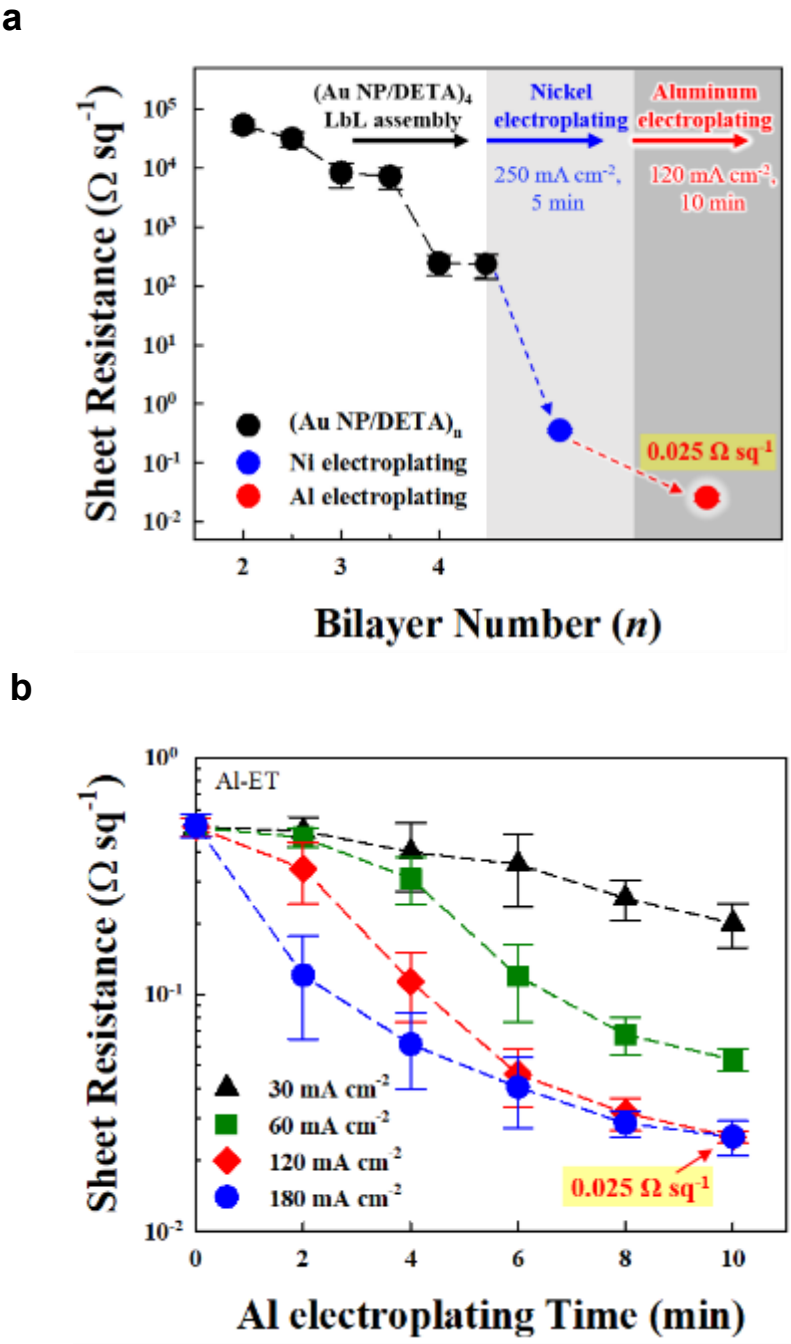

FIG. S7. (a) Sheet resistances of the (Au NP/DETA)$_{n=1-4}$ multilayer-coated polyester textiles as a function of bilayer number (n) and the Ni-ET. (b) Change in the sheet resistance values of the Al-ET as a function of electroplating current density and electroplating time.

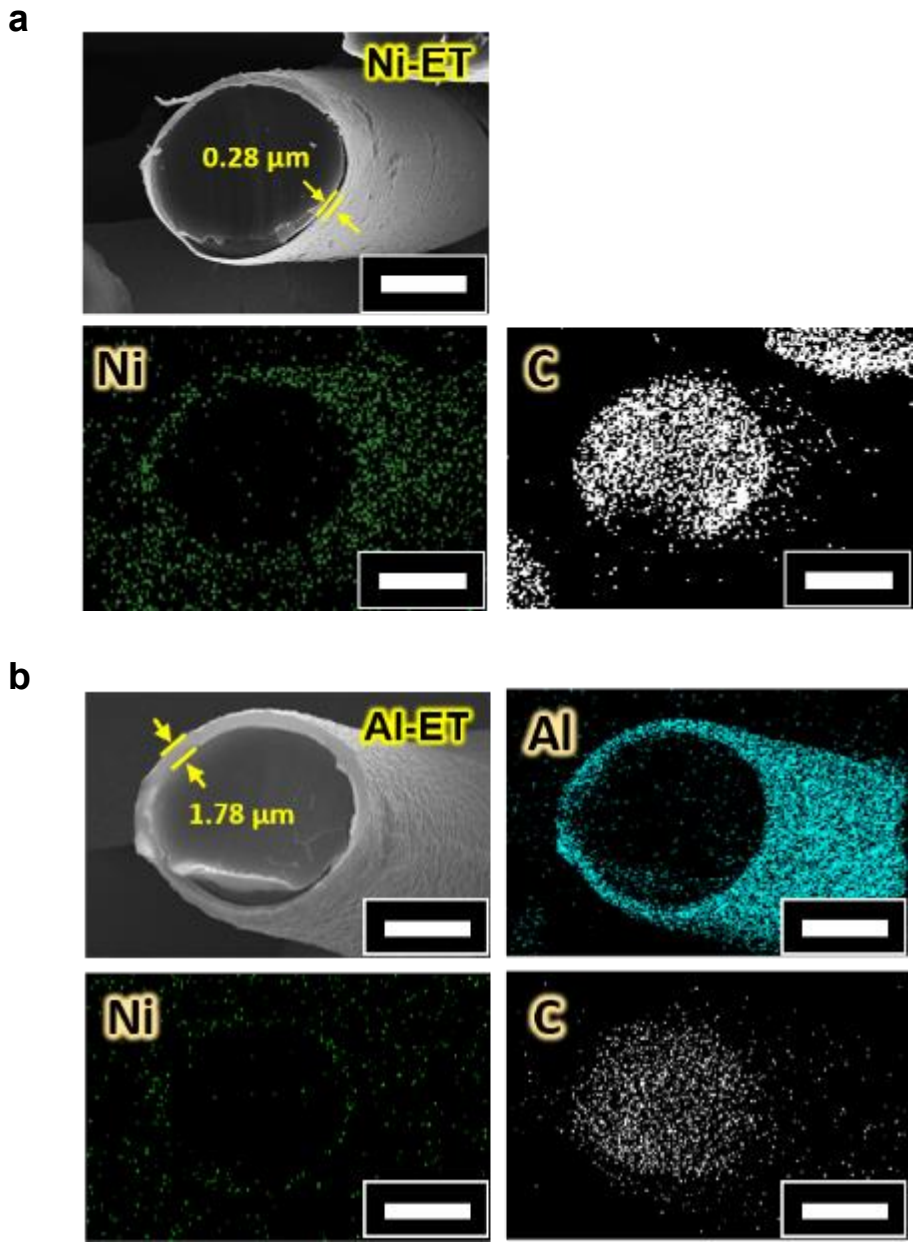

FIG. S8. Tilted and cross-sectional (inset) FE-SEM images (scale bar, 10 µm) and EDS mapping images (scale bar, 10 µm) of a fiber of (a) Ni-ET (electroplated Ni layer thickness ~0.28 µm) and (b) Al-ET (electroplated Al layer thickness ~1.78 µm). In the case of Ni-ET, Ni electroplating was performed onto the $(Au\ NP/DETA)_4$ multilayer-coated polyester for 5 min with current density of 250 mA cm^{-2} and for Al-ET, Al electroplating was sequentially conducted onto the Ni-ET for 10 min with current density of 120 mA cm^{-2}.

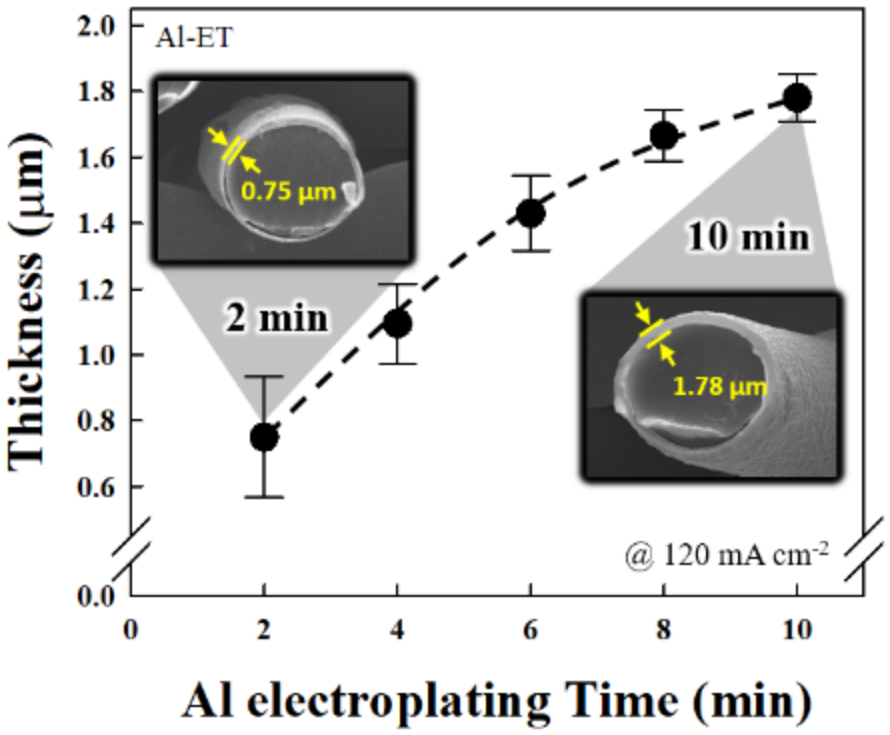

FIG. S9. Thickness data and FE-SEM images (insets) of the electroplated Al layer of fiber of the Al-ET as a function of electroplating time with current density of 120 mA cm^{-2}.

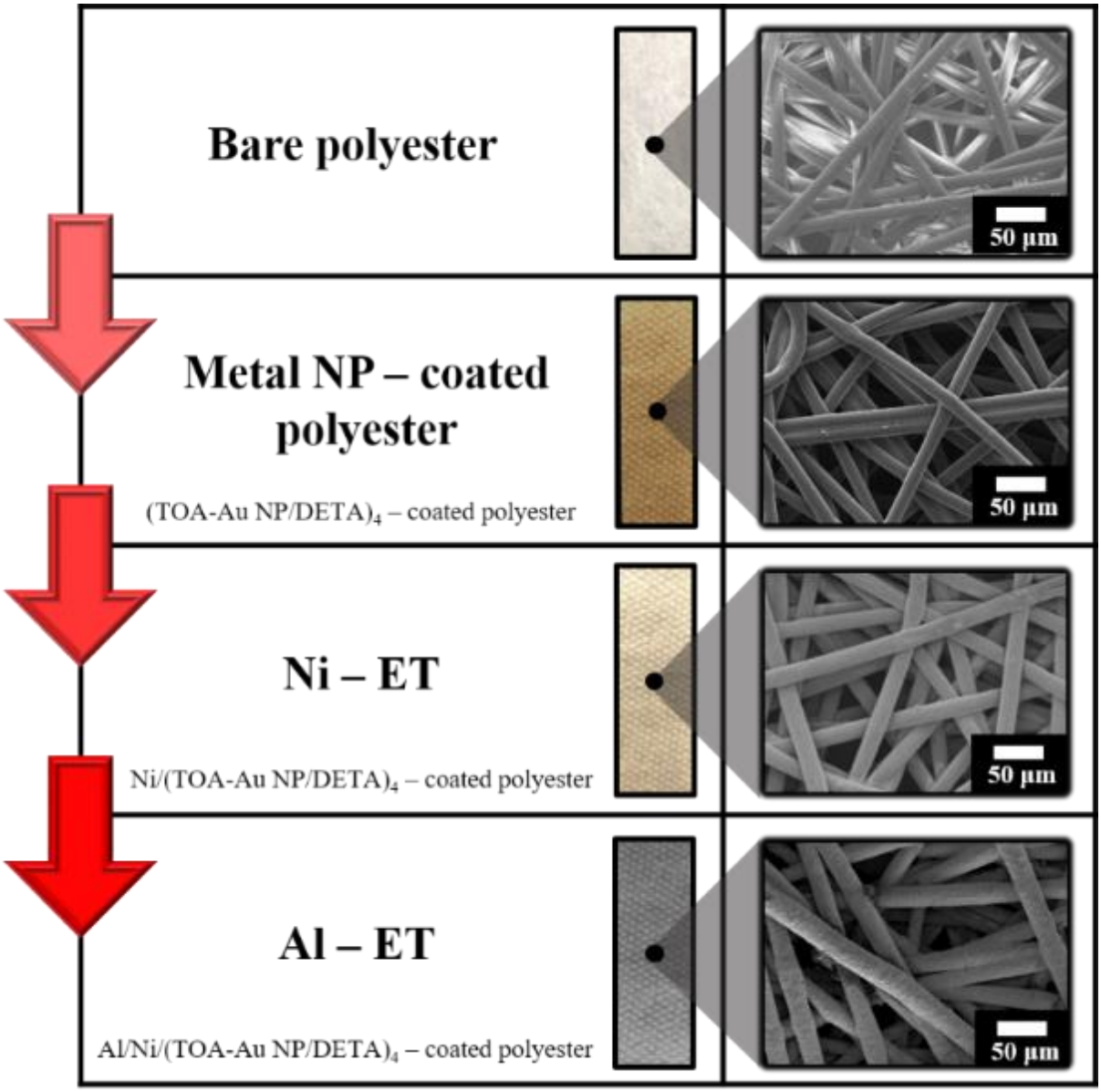

FIG. S10. Photographic and FE-SEM images of bare polyester, metal NP-coated polyester, Ni-ET, and Al-ET. In the case of Ni-ET, Ni electroplating was performed onto the $(Au\ NP/DETA)_4$ multilayer-coated polyester for 5 min with current density of 250 mA cm^{-2} and for Al-ET, Al electroplating was sequentially conducted onto the Ni-ET for 10 min with current density of 120 mA cm^{-2}.

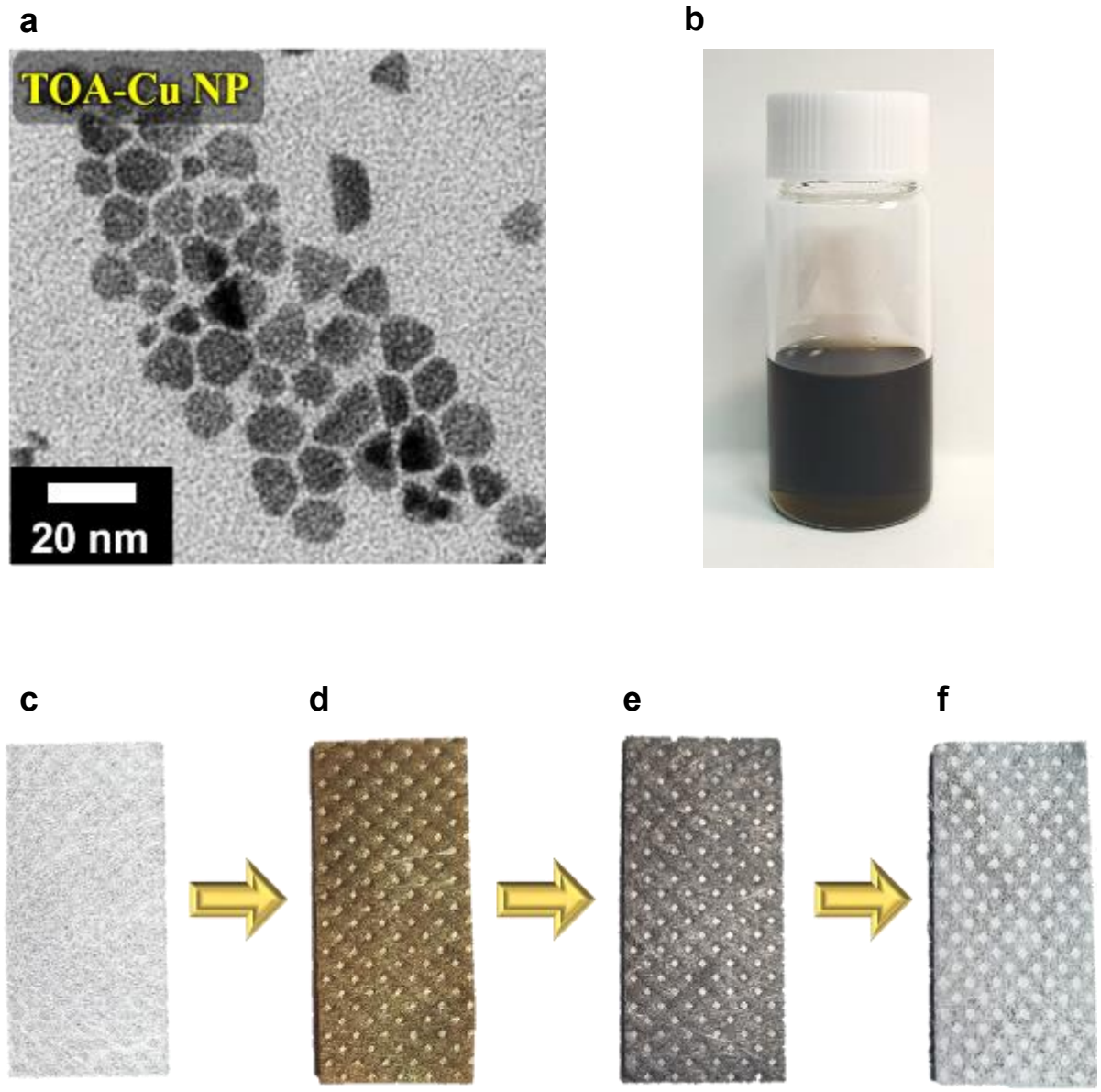

FIG. S11. (a) HR-TEM images of TOA-Cu NP with a diameter of approximately 10 nm. Photographic images of (b) TOA-Cu NP solution (in toluene) and (c) bare, (d) Cu NP-coated, (e) Ni-electroplated, and (f) Al-electroplated polyester textile.

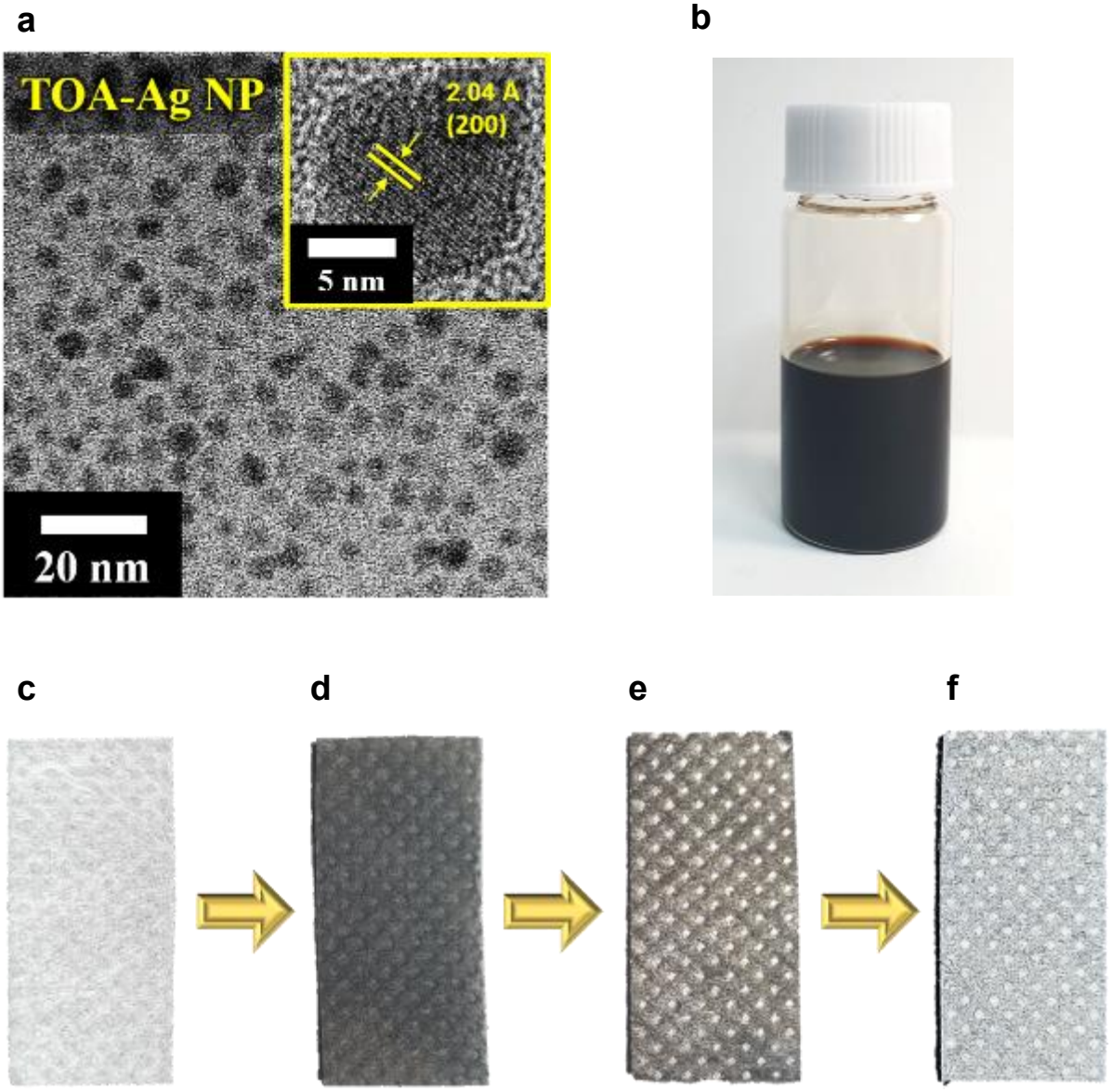

FIG. S12. (a) HR-TEM images of TOA-Ag NP with a diameter of approximately 8.5 nm. Photographic images of (b) TOA-Ag NP solution (in toluene) and (c) bare, (d) Ag NP-coated, (e) Ni-electroplated, and (f) Al-electroplated polyester textile.

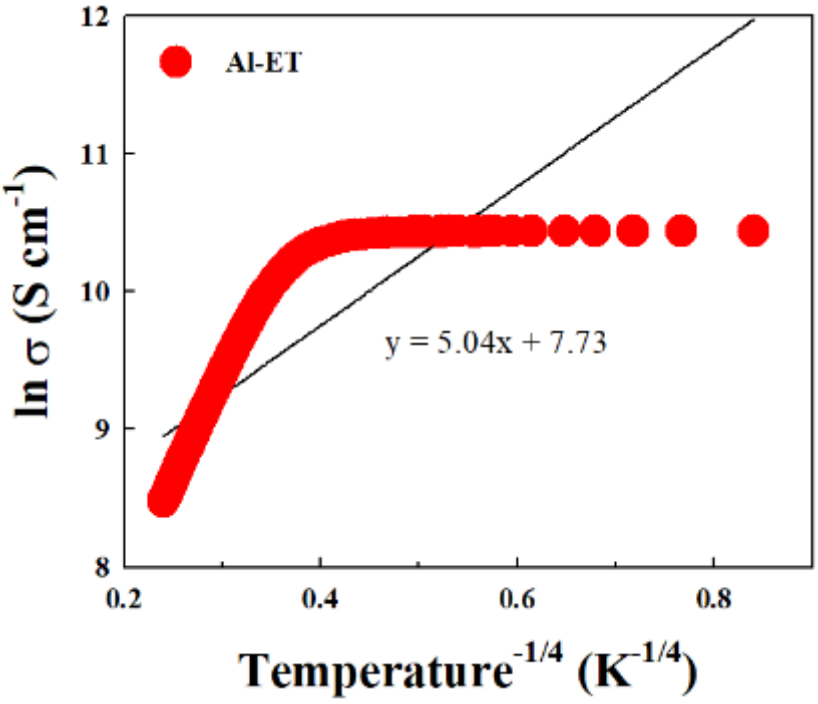

FIG. S13. The plot of $ln\sigma$ vs $T^{-1/4}$ (for hopping) of Al-ET.

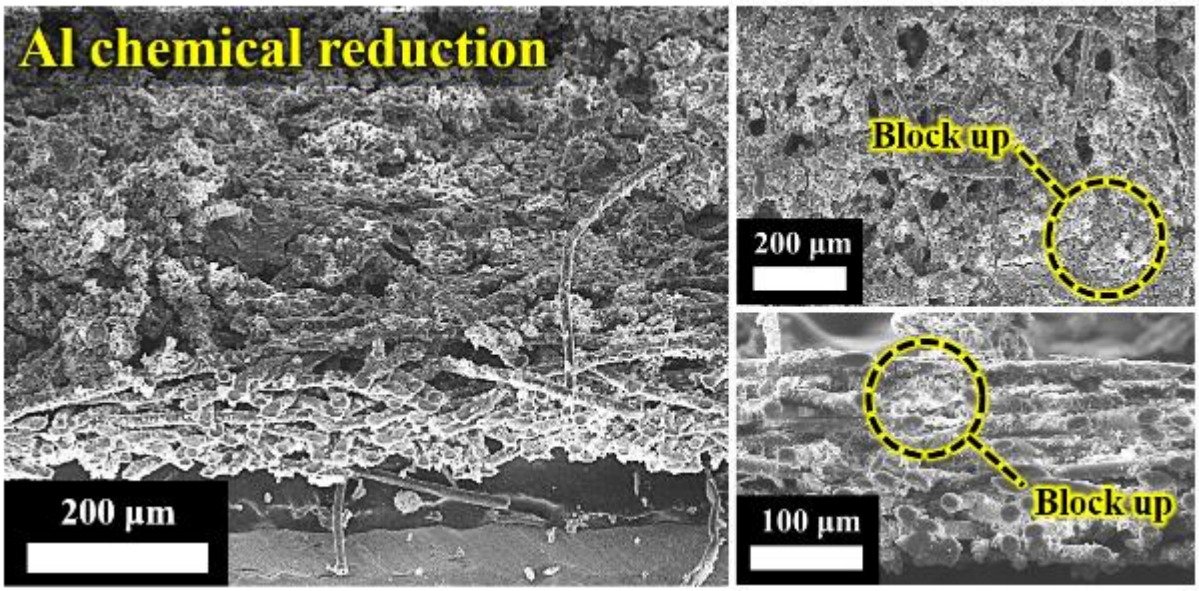

FIG. S14. FE-SEM images of electroless Al-coated polyester prepared from aluminum ion reduction method. In this case, electroless Al layer was nonuniformly coated onto the polyester textiles, generating the block-up of porosities within textiles.

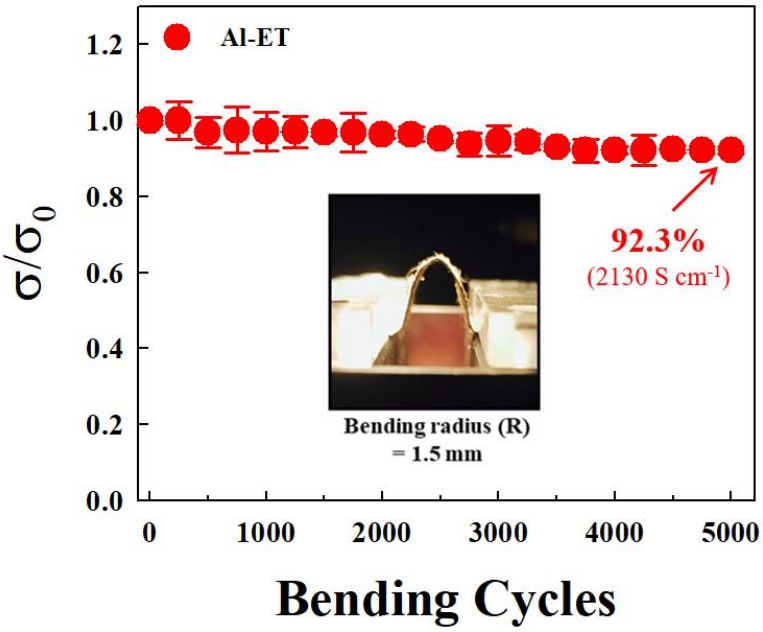

FIG. S15. Relative electrical conductivity of Al-ET as a function of bending cycles.

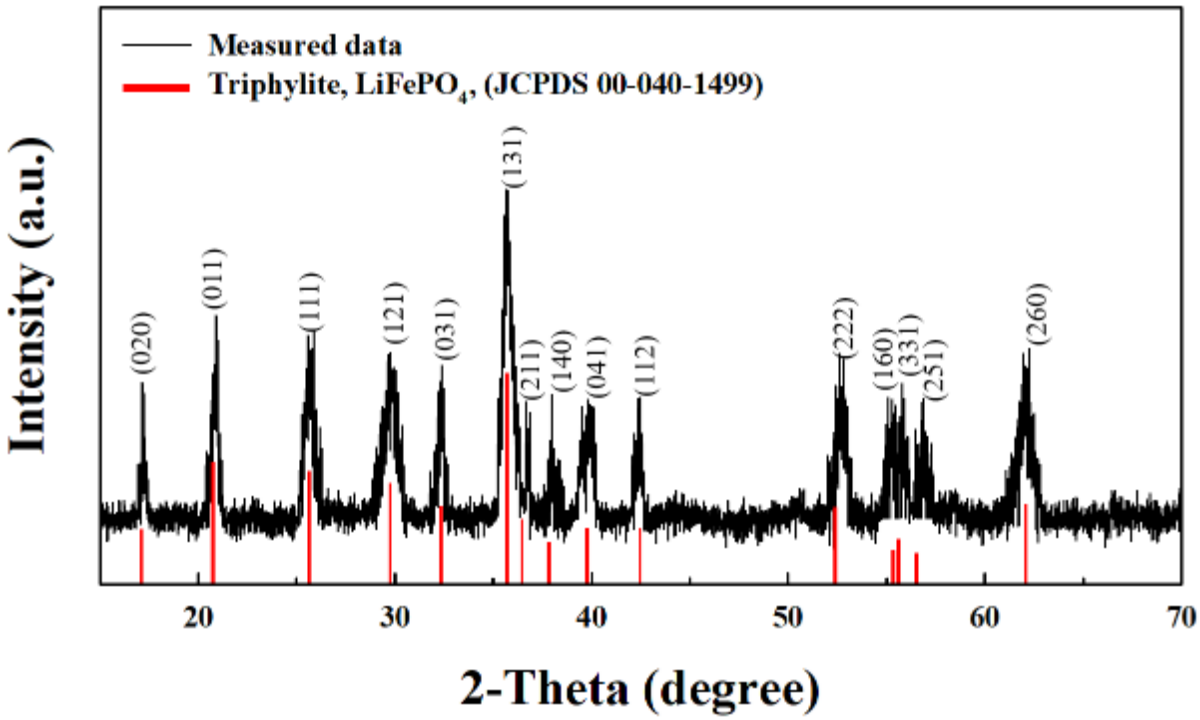

FIG. S16. XRD data of synthesized LFP NP. The XRD pattern of the LFP NPs exhibited the same intensity distribution of the olivine structured-bulk materials (JCPDS 00-040-1499).

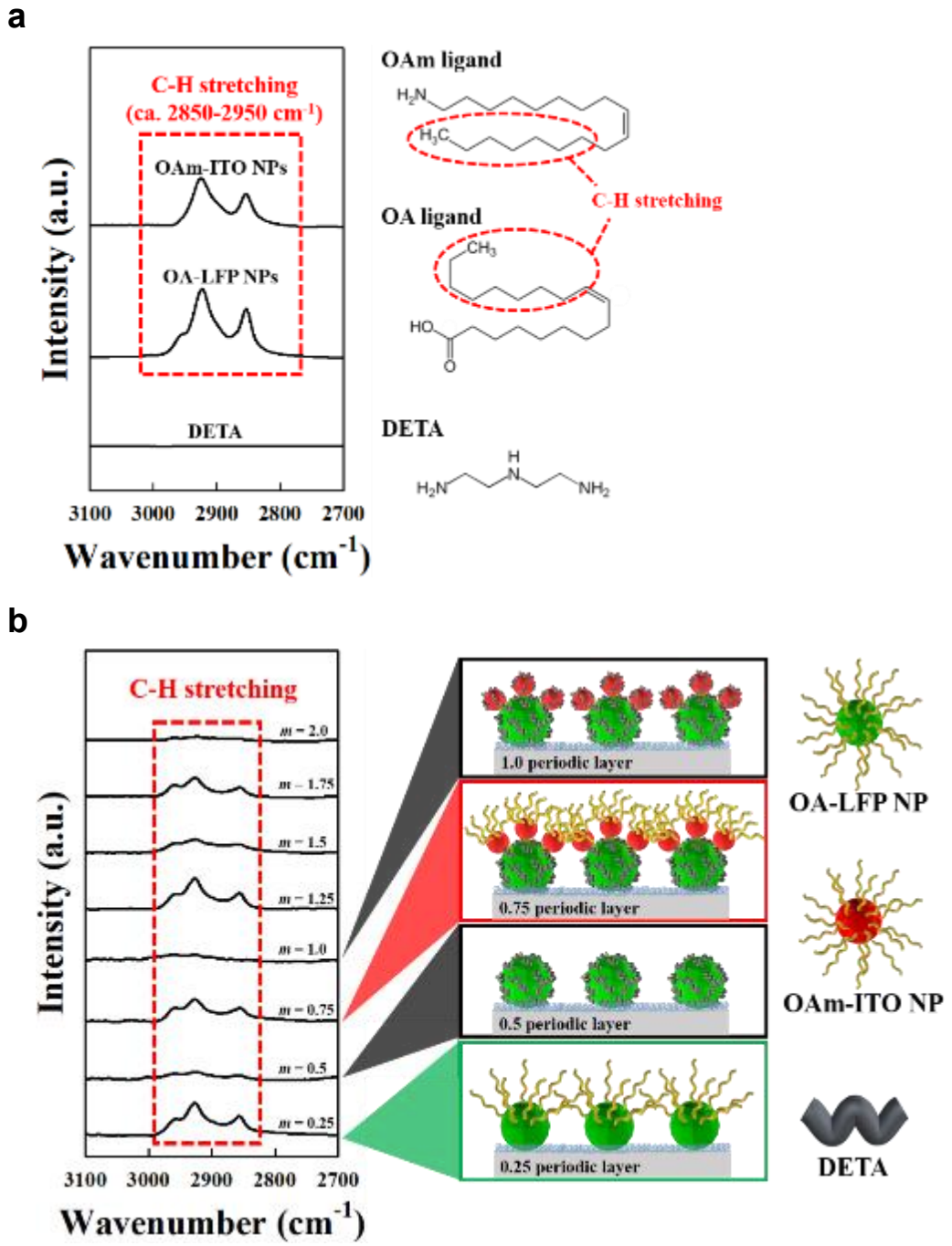

FIG. S17. (a) FT-IR spectra of pristine OAm-ITO NP, OA-LFP NP and DETA. The C—H stretching peaks in the range of 3000 - 2850 cm^{-1} originate from long alkyl chains of bulky OAm and OA ligands. (b) FTIR spectra and scheme of ligand-exchange LbL-assembled $(DETA/OAm\text{-}ITO\ NP/DETA/OA\text{-}LFP\ NP)_n$ multilayers as a function of the bilayer number (*n*). As shown in the FTIR spectra of Figure S2b, the deposition of DETA onto the OA-LFP NP-coated-substrates removed the bulky OA ligands (see the C-H stretching peaks at 2,850 − 2,950 cm^{-1}) loosely bound to the surface of the LFP NPs, and at the same time, DETA was

directly adsorbed onto the surface of the LFP NPs, which was confirmed by the disappearance of the C-H stretching peaks (at 3000 – 2850 cm^{-1}) originating from bulky OA ligands (see m = 0.5 in **Fig. S15(b)**). Furthermore, these similar phenomena were also observed when the DETA was deposited onto the OAm-ITO NP-coated substrates (see m = 1.0 in **Fig. S15(b)**). As a result, the alternating deposition of DETA, OA-LFP NPs, DETA, and OAm-ITO NPs repeated the generation and disappearance of the C-H stretching peaks (at 3000 – 2850 cm^{-1}) originating from the OA and OAm ligands when the outermost layer was changed from DETA to OA-LFP or OAm-ITO NPs and vice versa.

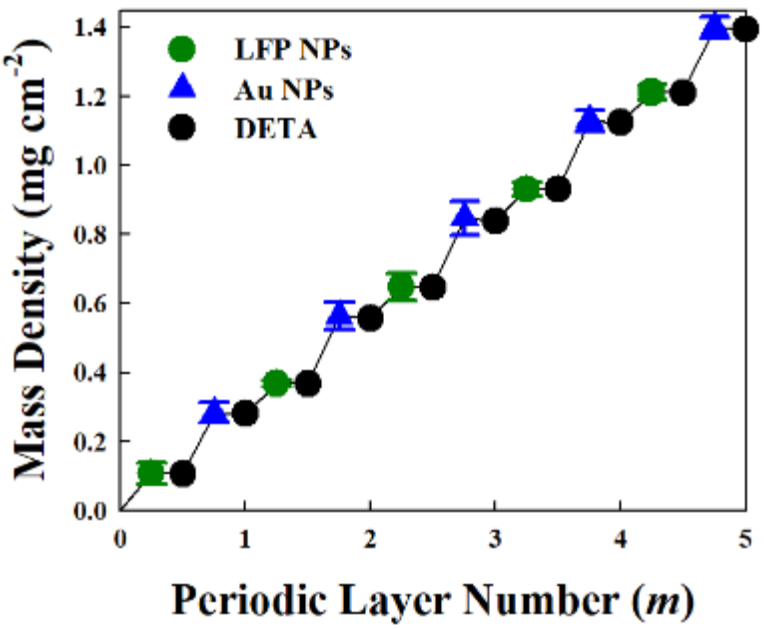

FIG. S18. Loading mass density data of the (LFP NP/DETA/Au NP/DETA)$_m$ multilayers coated onto Al-ET as function of periodic layer number (*m*).

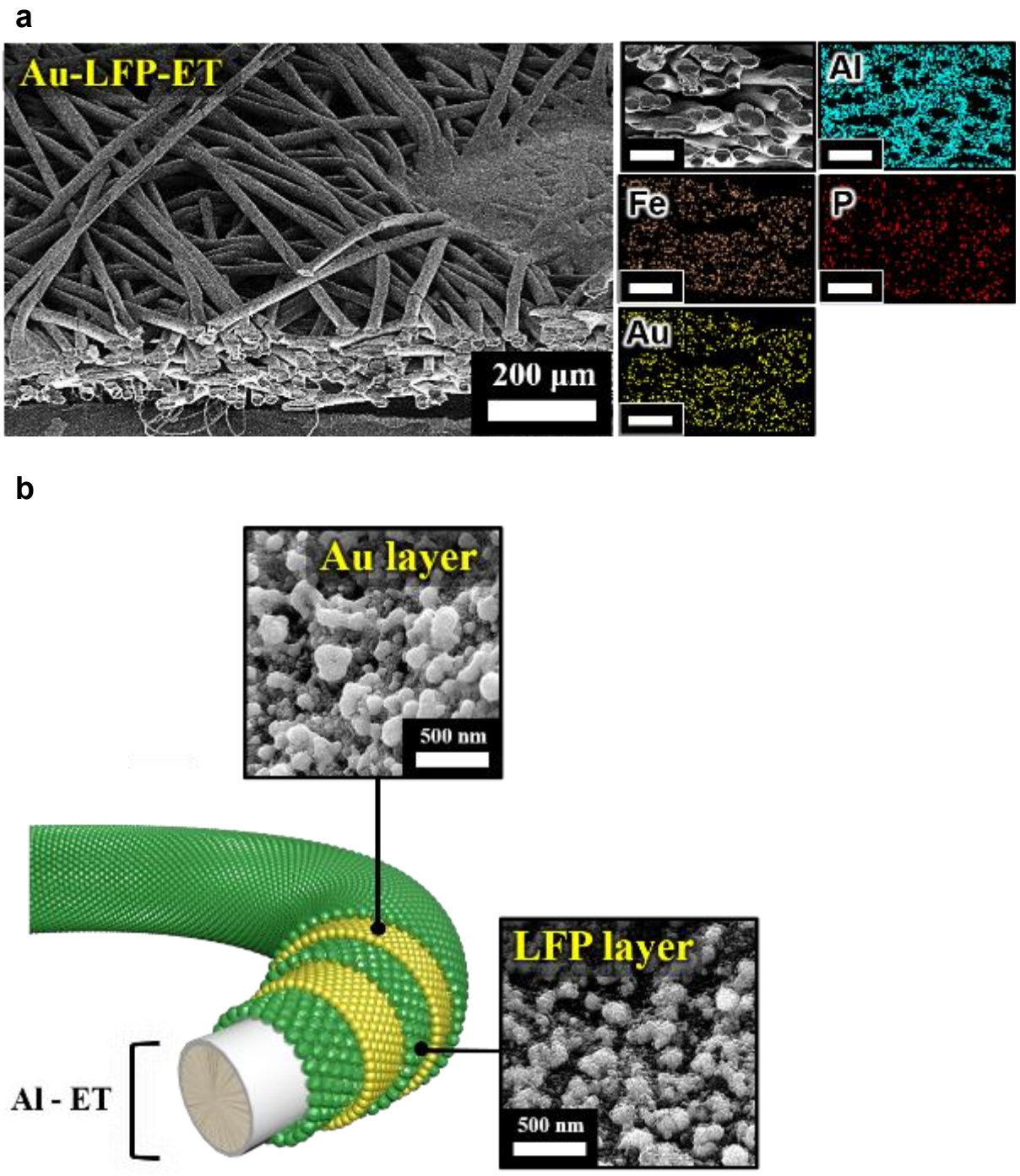

FIG. S19. (a) Tilted and cross-sectional (inset) FE-SEM images (scale bar, 50 μm (inset)) and EDS mapping images (scale bar, 50 μm) of Au-LFP-ET. (b) Schematic illustration and SEM of outermost layer of Au-LFP-ET. The respective NPs were uniformly deposited onto all the regions (from the exterior to interior regions) of Al-ET.

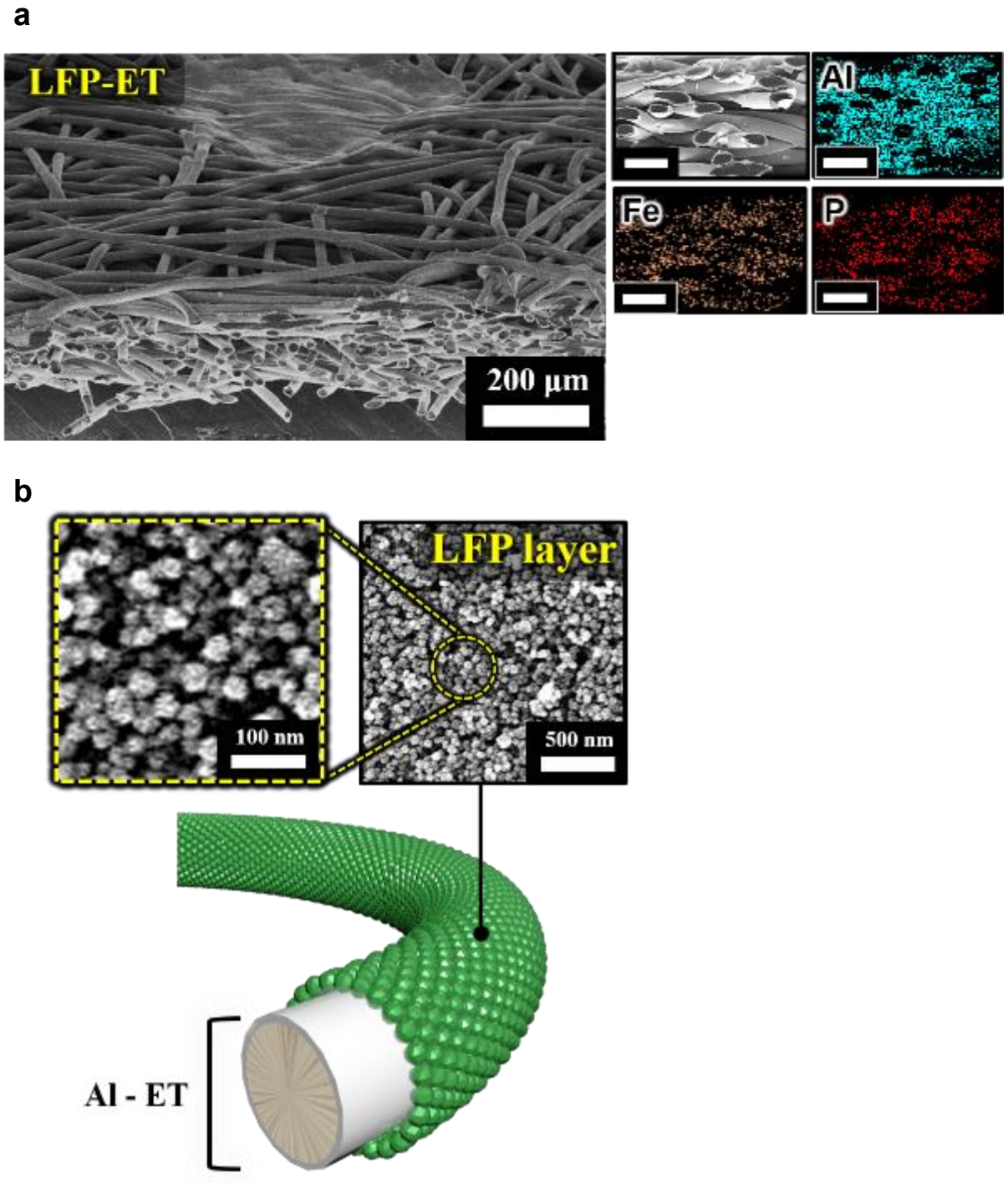

FIG. S20. (a) Tilted and cross-sectional (inset) FE-SEM images (scale bar, 50 μm (inset)) and EDS mapping images (scale bar, 50 μm) of LFP-ET. (b) Schematic illustration and SEM of outermost layer of LFP-ET. The respective NPs were uniformly deposited onto all the regions (from the exterior to interior regions) of Al-ET.

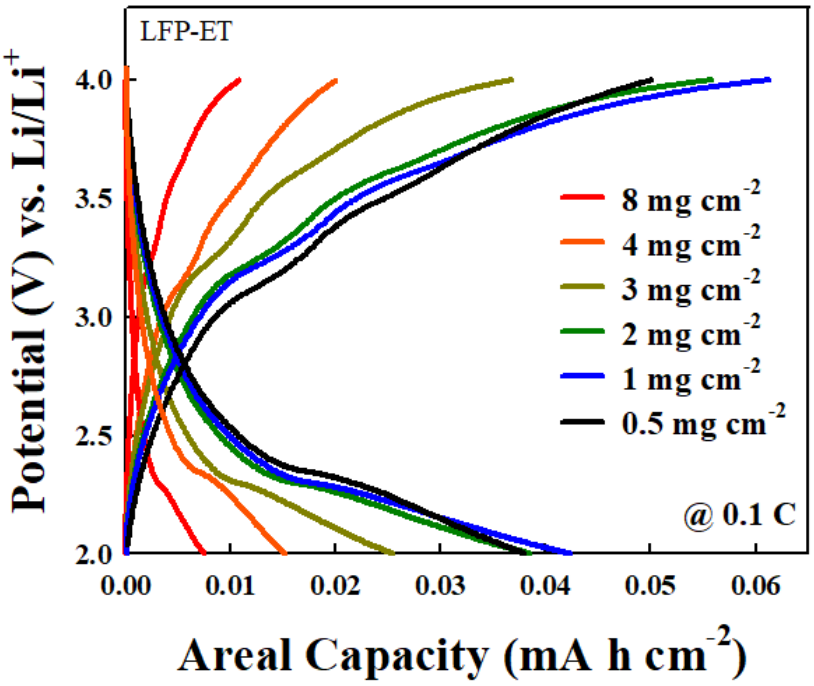

FIG. S21. GCD profiles (at 0.1 C) of LFP-ET electrode with loading mass density LFP NP ranging from 0.5 to 8 mg cm^{-2}

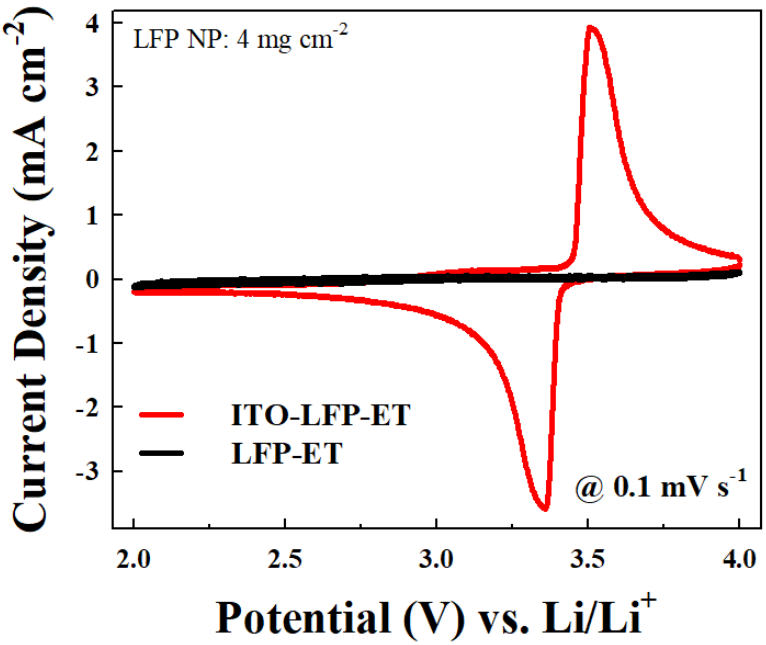

FIG. S22. CV curves of ITO-LFP-ET and LFP-ET at a scan rate of 0.1 mV s^{-1}. The loading mass densities of LFP NP in two different samples were fixed at 4 mg cm^{-2}.

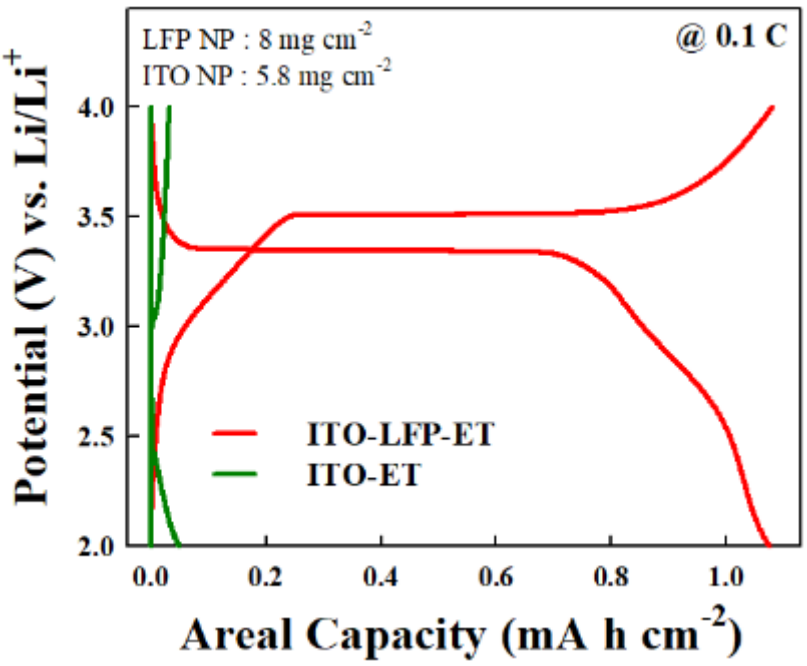

FIG. S23. GCD profiles of ITO-LFP-ET electrode with 8 mg cm^{-2} of LFP NP, 5.8 mg cm^{-2} of ITO NP and ITO-ET (i.e., $(ITO\ NP/DETA)_m$-coated Al-ET) electrode with 5.8 mg cm^{-2} of ITO NP at 0.1 C. In this case, ITO-ET electrode exhibited areal capacity of 0.0481 mA h cm^{-2} (approximately 4.5% of areal capacity of the ITO-LFP-ET electrode with same amount of ITO NP)

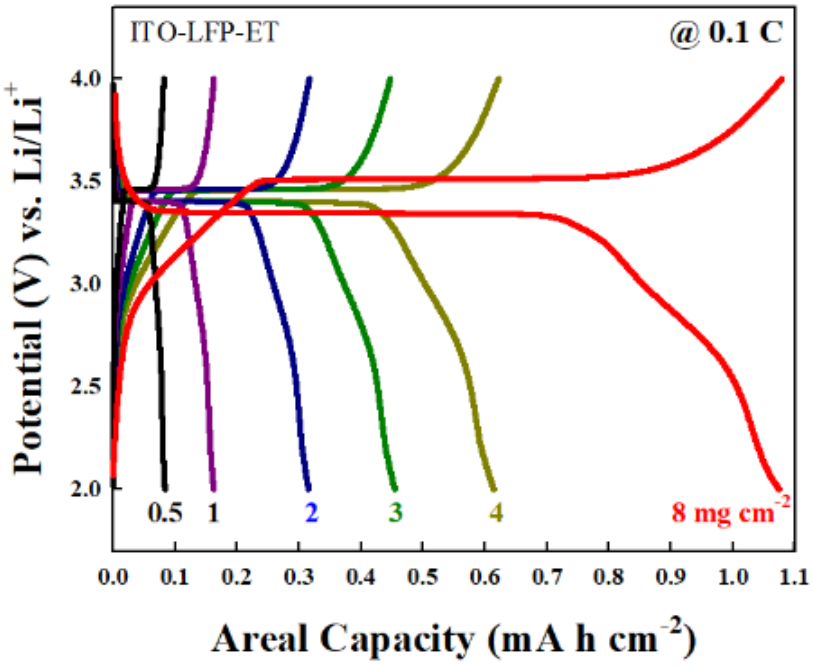

FIG. S24. GCD profiles (at 0.1 C) of ITO-LFP-ET electrode with loading mass density LFP NP ranging from 0.5 to 8 mg cm^{-2}

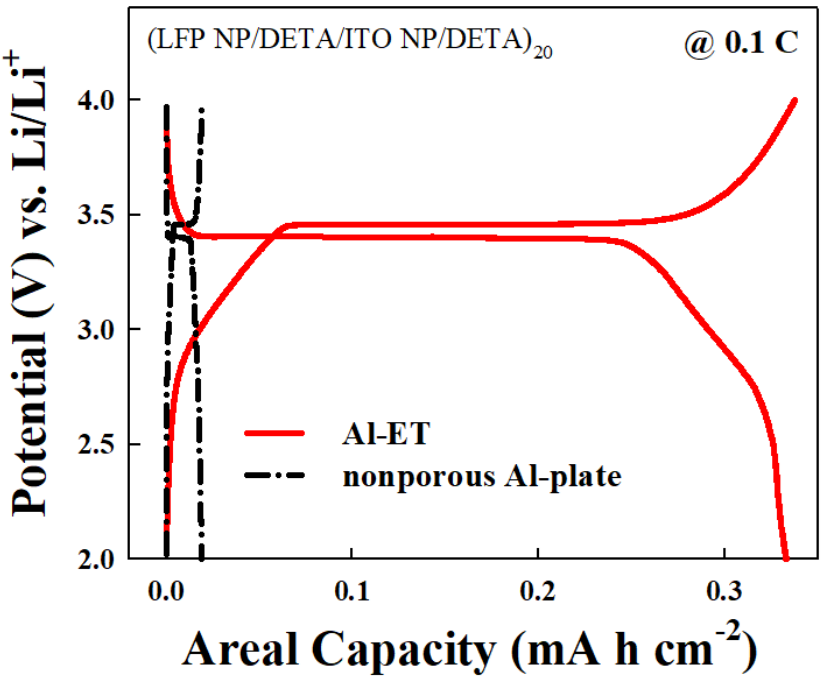

FIG. S25. GCD profiles of (LFP NP/DETA/ITO NP/DETA)$_{20}$ multilayers deposited onto Al-ET and nonporous Al-plate.

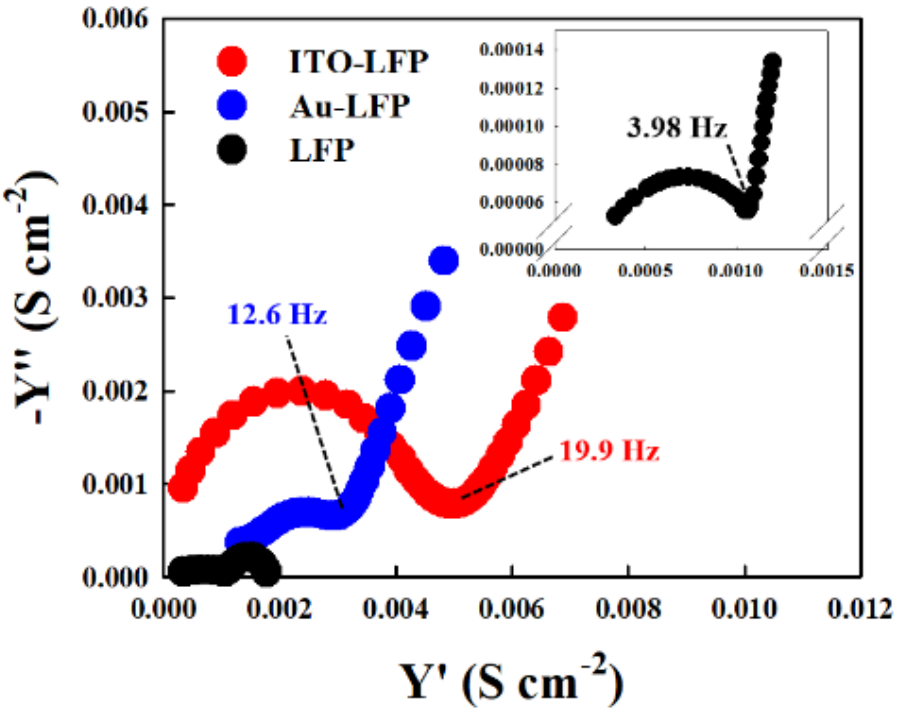

FIG. S26. Admittance plot of ITO-LFP-ET, Au-LFP-ET, and LFP-ET electrode with 4 mg cm^{-2} of LFP NP for the charge transfer rate related to the diffusion distance with knee frequency.

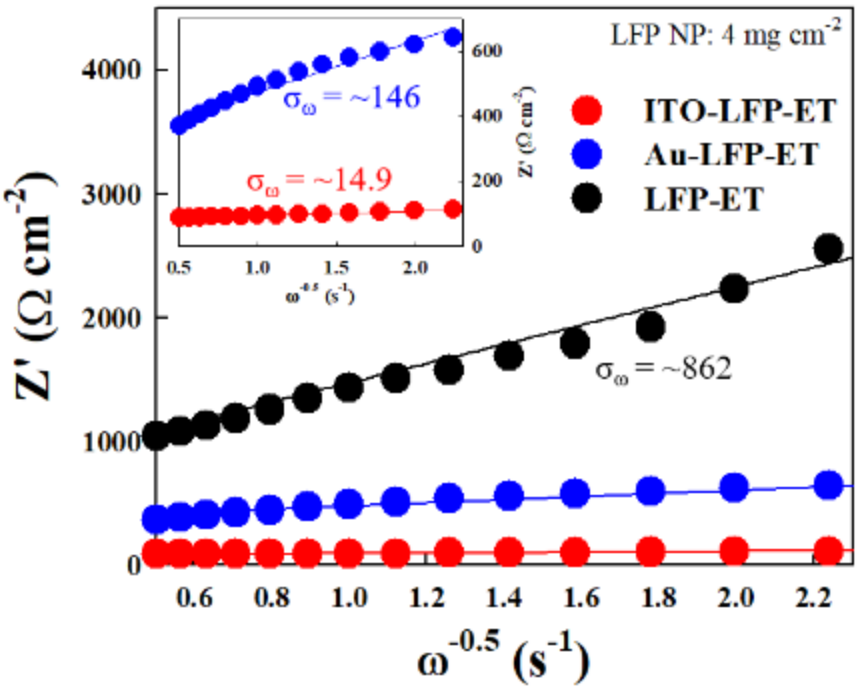

FIG. S27. Warburg impedance coefficient plot of ITO-LFP-ET, Au-LFP-ET, and LFP-ET electrode with 4 mg cm^{-2} of LFP NP.

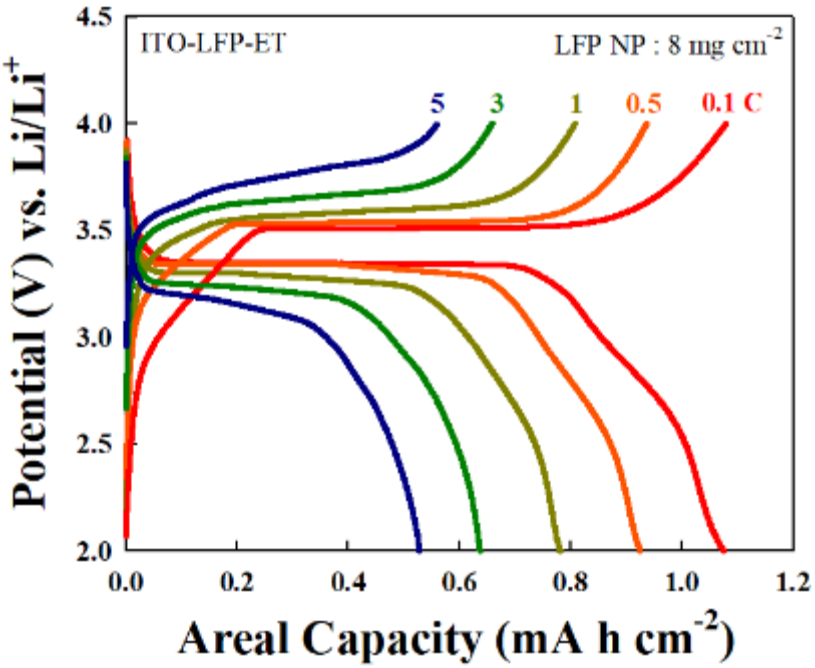

FIG. S28. GCD profiles of ITO-LFP-ET electrode with a loading mass density of LFP NP ~ 8 mg cm^{-2} at various current densities.

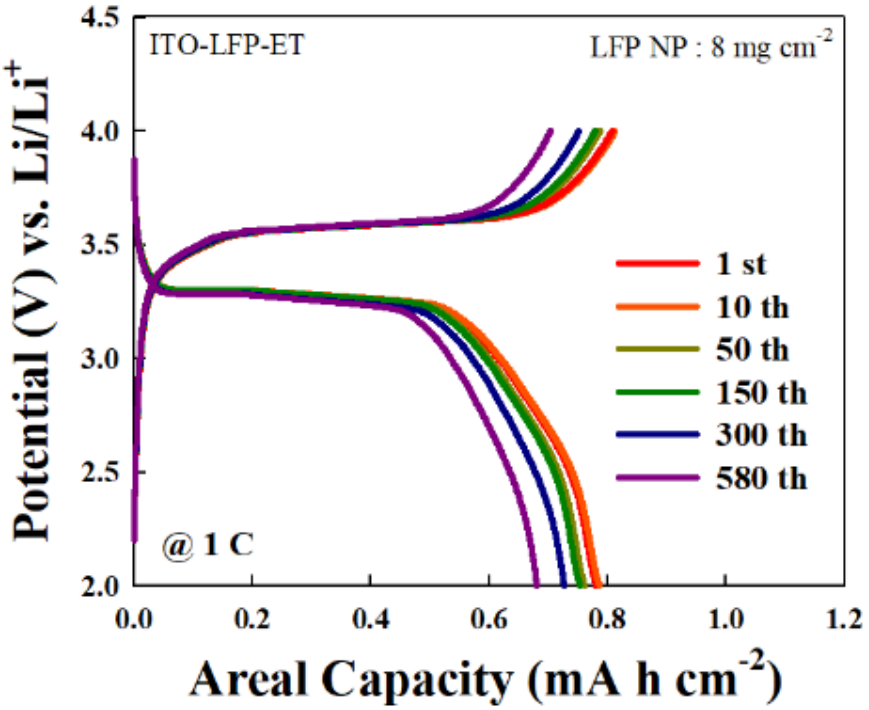

FIG. S29. GCD profiles of ITO-LFP-ET electrode with a loading mass density of LFP NP ~ 8 mg cm^{-2} at different charge-discharge cycles.

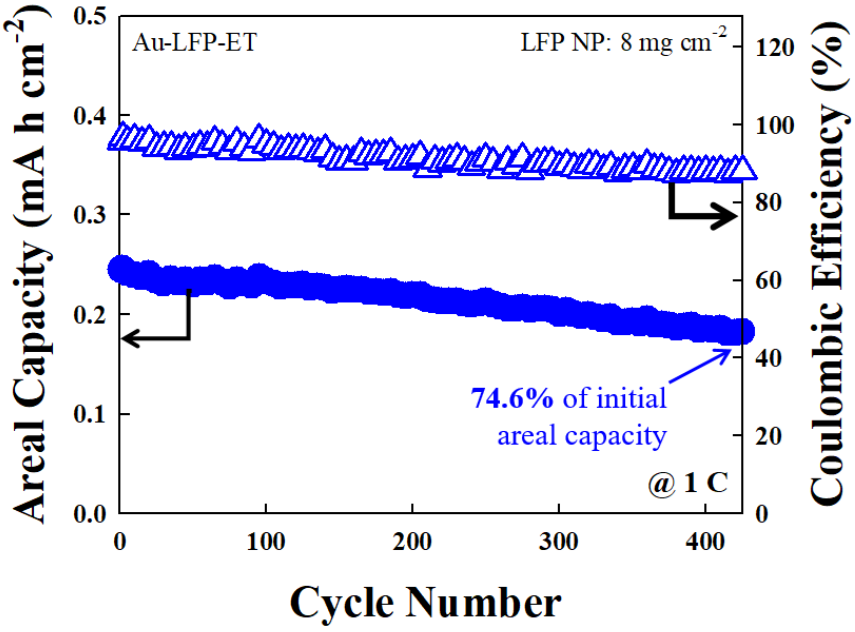

FIG. S30. Cycling retention and Coulombic efficiency of Au-LFP-ET electrodes with loading mass densities of 8 mg cm^{-2} obtained at 1 C.

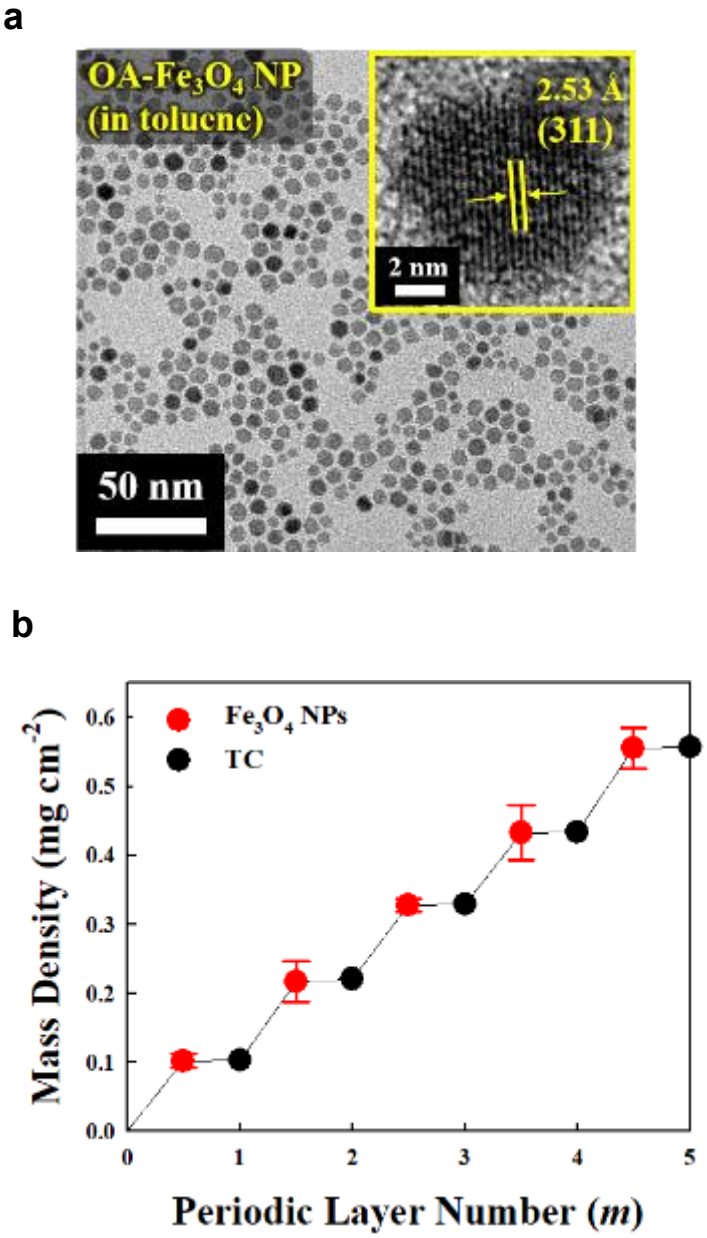

FIG. S31. (a) HR-TEM images of OA-Fe_3O_4 NPs. (b) Loading mass density data of the $(Fe_3O_4$ NP/TC$)_m$ multilayers coated onto Ni-ET as function of periodic layer number (m). In this system, the mass loading densities of Fe_3O_4 NPs were measured to be ~0.113 mg cm^{-2} per layer, respectively.

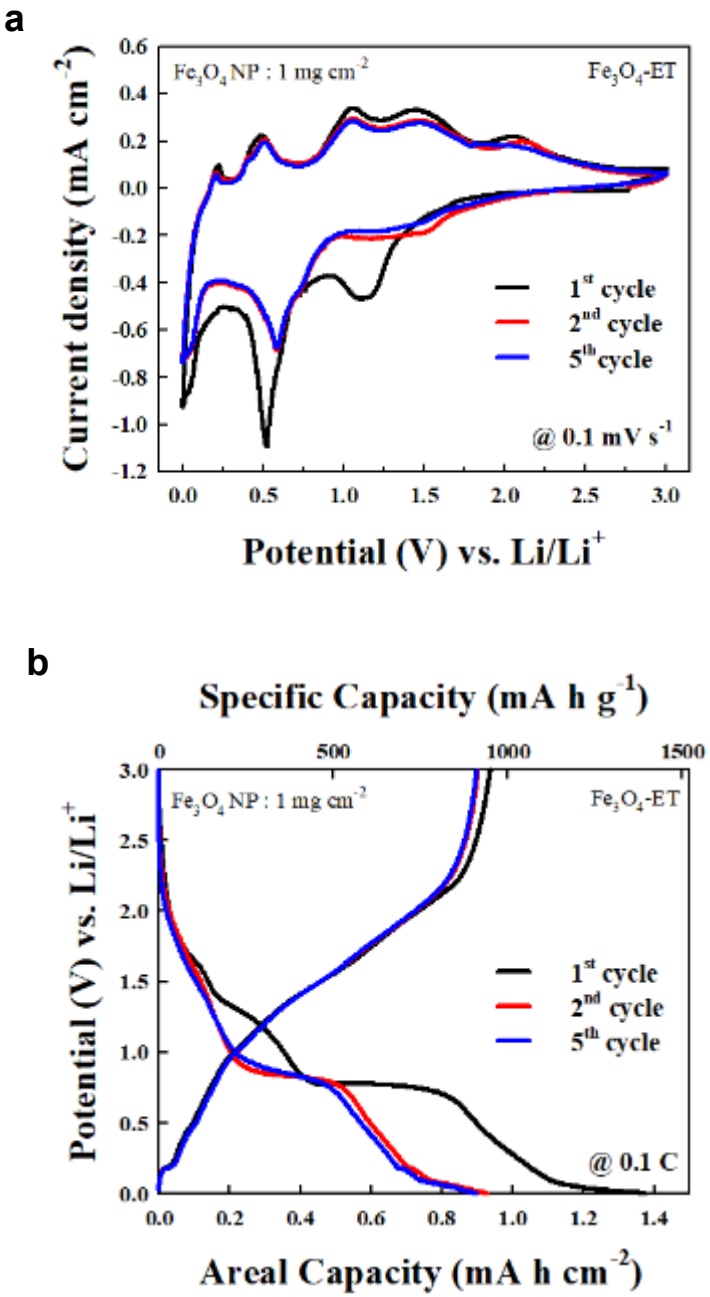

FIG. S32. (a) CV curves and (b) GCD profiles of Fe_3O_4-ET (i.e., $(Fe_3O_4$ NP/DETA$)_m$-coated Ni-ET) electrode with a loading mass density of Fe_3O_4 NP ~ 4 mg cm^{-2} at different charge-discharge cycles.

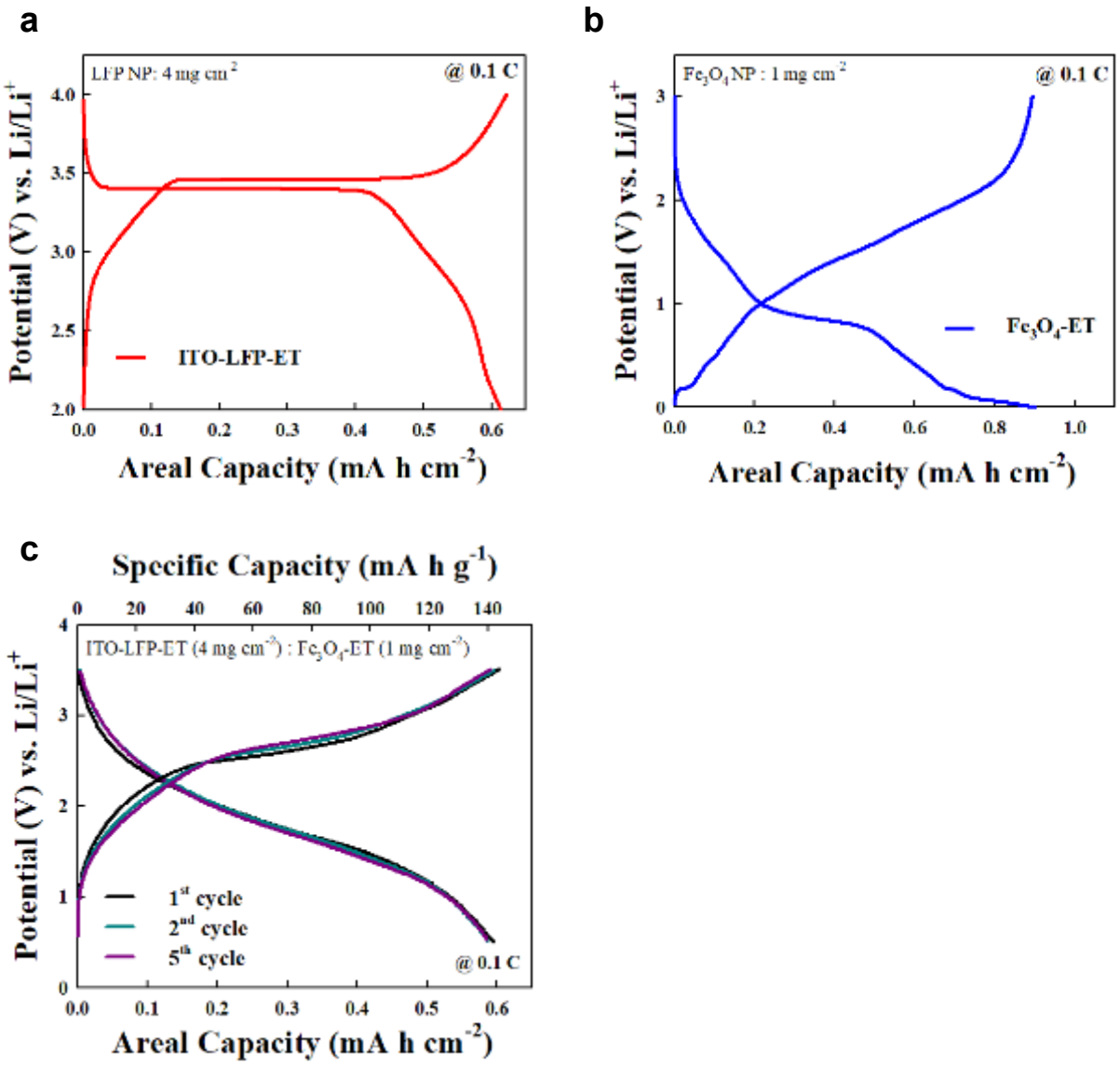

FIG. S33. GCD profiles of (a) ITO-LFP-ET electrode with a loading mass density of LFP NP ~ 4 mg cm^{-2}, (b) Fe_3O_4-ET electrode with a loading mass density of Fe_3O_4 NP ~ 1 mg cm^{-2}, and (c) full cell electrode composed of ITO-LFP-ET (4 mg cm^{-2} of LFP NP) as a cathode and Fe_3O_4-ET (1 mg cm^{-2} of Fe_3O_4 NP) as an anode at 0.1 C. The n/p ratio set for full cell assembly was approximately 1.44 and the voltage range was 0.5-3.5 V. In this case, areal capacity of the full cell was 0.584 mA h cm^{-2}.

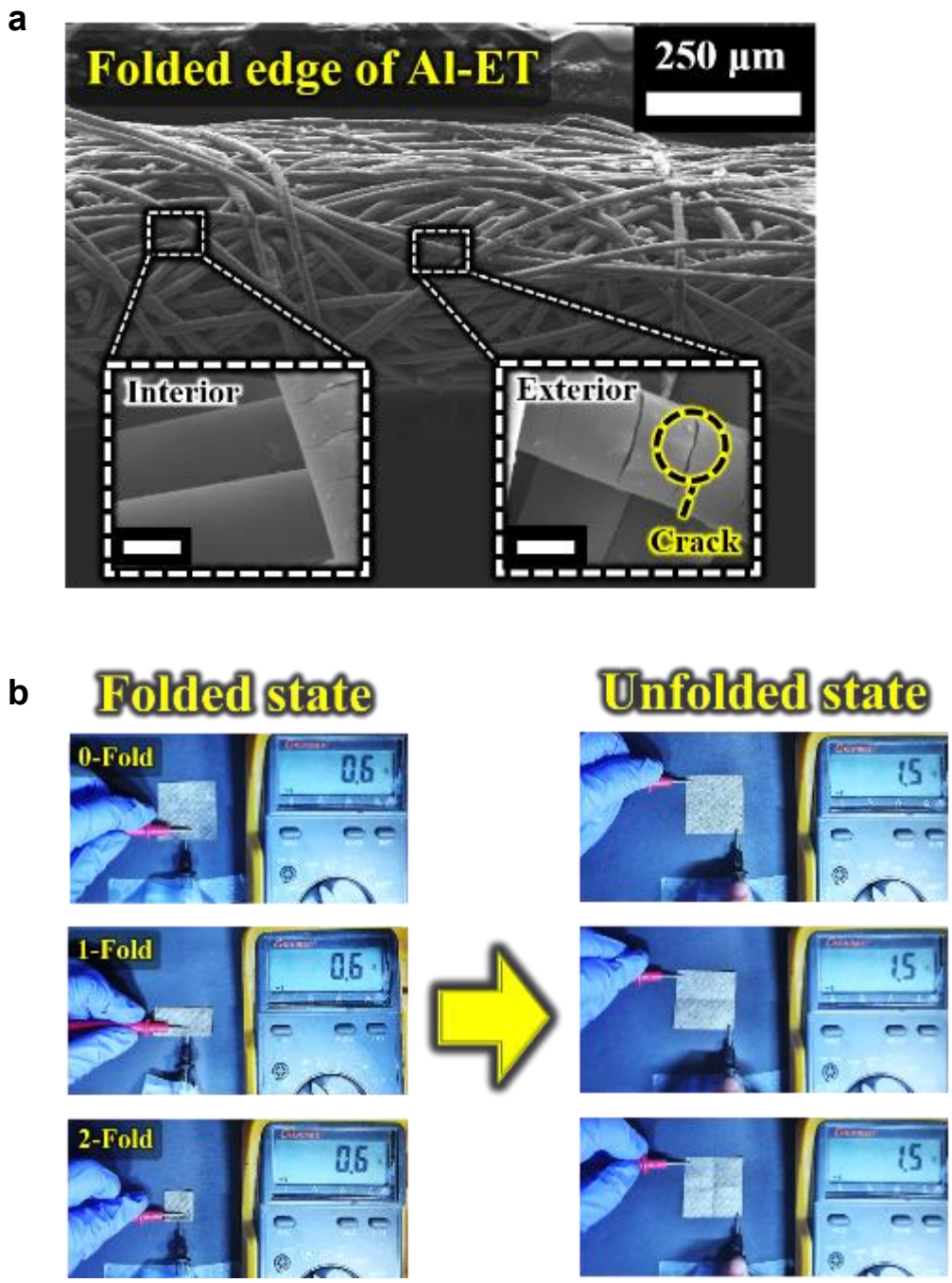

FIG. S34. (a) Cross-sectional FE-SEM image measured at 180°-folded edge of Al-ET. In this case, the uniform coating of electroplated Al layer onto the textiles was well preserved despite the formation of only partial cracks. (b) Photographic images showing the electrical properties of Al-ET at folded and unfolded states with increasing folding number. The unit of digital numbers measured from multi-tester was resistance (Ω).

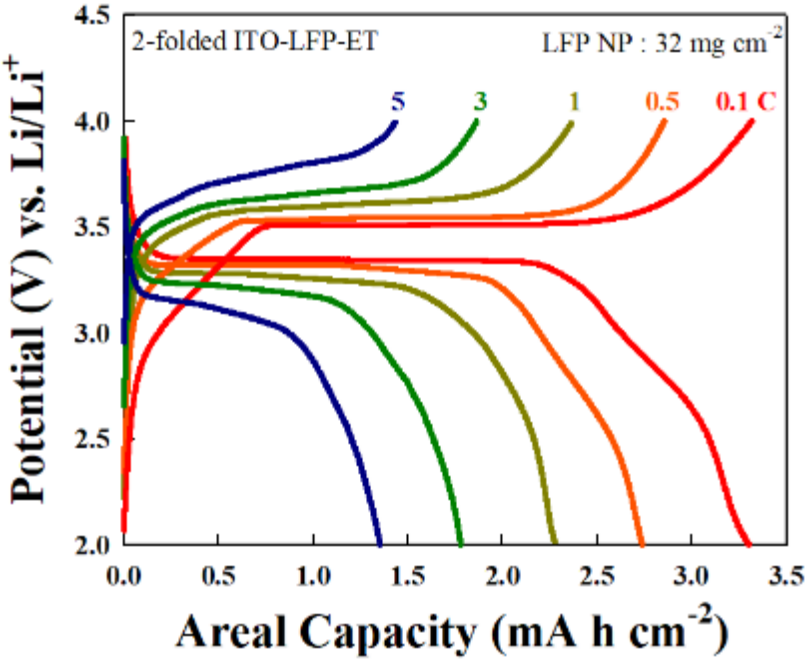

FIG. S35. GCD profiles of 2-folded ITO-LFP-ET electrode with a loading mass density of LFP NP ~ 32 mg cm^{-2} at various current densities.

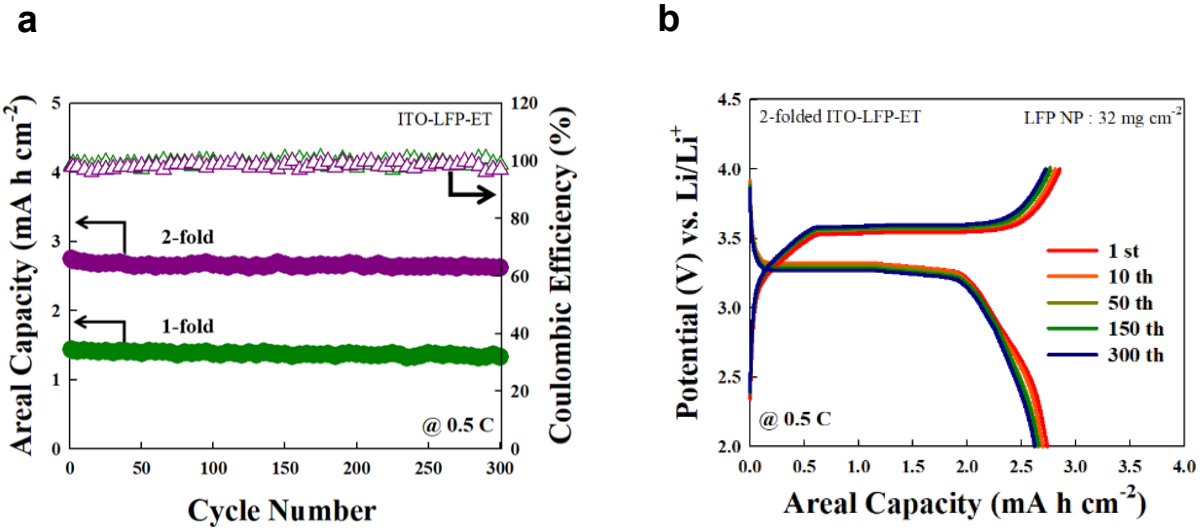

FIG. S36. (a) Cycling retention and Coulombic efficiency of 1- and 2-folded ITO-LFP-ET electrodes obtained at 0.5 C. (b) GCD profiles of 2-folded ITO-LFP-ET electrode with a loading mass density of LFP NP ~ 32 mg cm^{-2} at different charge-discharge cycles.

REFERENCES

[S1]X. Tu, J. Zhang, M. Zhang, Y. Cai, H. Lang, G. Tian and Y. Wang, RSC Adv. **7**(24), 14790 (2017).